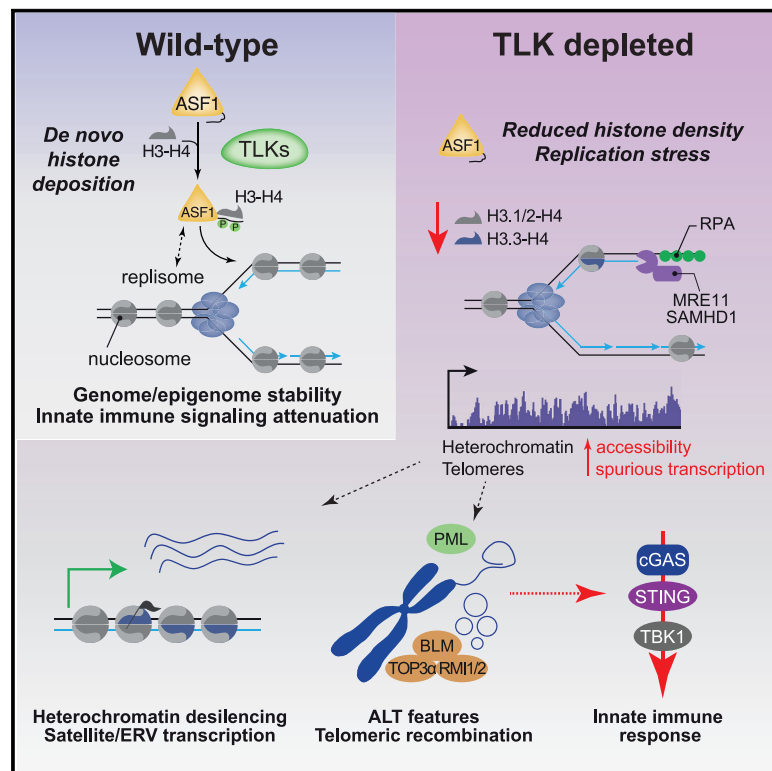


Tousled-Like Kinases Suppress Innate Immune Signaling Triggered by Alternative Lengthening of Telomeres

Graphical Abstract



Authors

Sandra Segura-Bayona,
Marina Villamor-Payà,
Camille Stephan-Otto Attolini,
Lars M. Koenig, Maria Sanchiz-Calvo,
Simon J. Boulton, Travis H. Stracker

Correspondence

sandra.segura-bayona@crick.ac.uk
(S.S.-B.),
travis.stracker@nih.gov (T.H.S.)

In Brief

Segura-Bayona et al. find the Tousled-like kinases (TLKs) maintain chromatin at repetitive genome elements and telomeres. TLK depletion results in heterochromatin desilencing and induction of alternative lengthening of telomeres (ALT), robustly activating cGAS-STING-TBK1-mediated innate immune responses. This suggests TLKs represent a druggable vulnerability in ALT+ and chromosomally unstable tumor cells.

Highlights

- TLK-deficient cells have increased accessibility at heterochromatin regions
- TLK1/2 suppress spurious transcription and telomere hyper-recombination
- Extra-telomeric DNA generated upon TLK loss promotes innate immune signaling
- cGAS-STING-TBK1 signaling in TLK-deficient cells is independent of replication stress



Article

Tousled-Like Kinases Suppress Innate Immune Signaling Triggered by Alternative Lengthening of Telomeres

Sandra Segura-Bayona,^{1,2,*} Marina Villamor-Payà,¹ Camille Stephan-Otto Attolini,¹ Lars M. Koenig,³ Maria Sanchiz-Calvo,¹ Simon J. Boulton,² and Travis H. Stracker^{1,4,5,*}

¹Institute for Research in Biomedicine (IRB Barcelona), The Barcelona Institute of Science and Technology, Barcelona 08028, Spain

²The Francis Crick Institute, 1 Midland Road, London NW1 1AT, UK

³Division of Clinical Pharmacology, University Hospital, LMU Munich, 80337 Munich, Germany

⁴Current address: Radiation Oncology Branch, National Cancer Institute, Bethesda, MD 20892, USA

⁵Lead Contact

*Correspondence: sandra.segura-bayona@crick.ac.uk (S.S.-B.), travis.stracker@nih.gov (T.H.S.)

<https://doi.org/10.1016/j.celrep.2020.107983>

SUMMARY

The Tousled-like kinases 1 and 2 (TLK1/2) control histone deposition through the ASF1 histone chaperone and influence cell cycle progression and genome maintenance, yet the mechanisms underlying TLK-mediated genome stability remain uncertain. Here, we show that TLK loss results in severe chromatin decompaction and altered genome accessibility, particularly affecting heterochromatic regions. Failure to maintain heterochromatin increases spurious transcription of repetitive elements and induces features of alternative lengthening of telomeres (ALT). TLK depletion culminates in a cGAS-STING-TBK1-mediated innate immune response that is independent of replication-stress signaling and attenuated by the depletion of factors required to produce extra-telomeric DNA. Analysis of human cancers reveals that chromosomal instability correlates with high TLK2 and low STING levels in many cohorts. Based on these findings, we propose that high TLK levels contribute to immune evasion in chromosomally unstable and ALT+ cancers.

INTRODUCTION

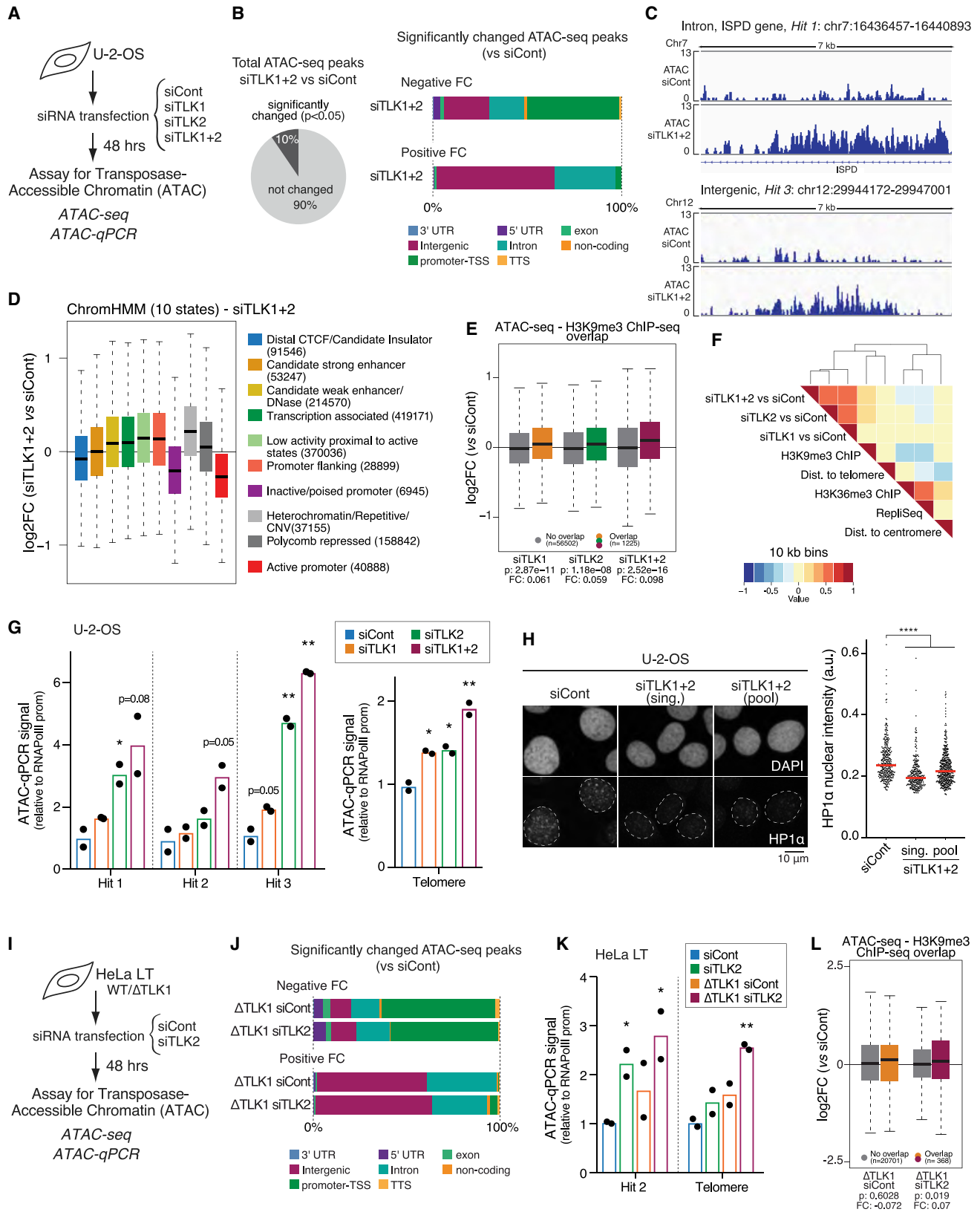
During early tumorigenesis, oncogene-driven unscheduled DNA replication causes replication stress (RS), a state characterized by slowed or stalled replication forks, increased single-stranded DNA (ssDNA) and activation of the DNA damage response (DDR) (Bartkova et al., 2005; Gorgoulis et al., 2005). DDR signaling acts as an inducible barrier to cancer progression, setting up a selective pressure for tumors to bypass the DDR. Unscheduled S-phase entry can generate an environment where nucleotides, replication factors, or histones are limiting (Bester et al., 2011; Halazonetis et al., 2008; Lee et al., 2018b). Oncogenes can also induce the firing of replication origins within highly transcribed genes, leading to replication-transcription conflicts that can drive chromosomal rearrangements (Kotsantis et al., 2018; Macheret and Halazonetis, 2018).

Tumor cells with high levels of chromosomal instability (CIN) and RS depend on the ATM and RAD3-related (ATR) and Checkpoint kinase 1 (CHK1) kinases to maintain CIN and RS at sub-toxic levels (Murga et al., 2011; Toledo et al., 2011). The dynamic maintenance of chromatin structure is required to maintain both genome and epigenome stability, and it regulates cell fate determination (Alabert et al., 2017; Yadav et al., 2018). ATR/CHK1-mediated DDR signaling is linked to the maintenance of chromatin structure through regulation of tousled-like kinase (TLK)

activity (Groth et al., 2003; Krause et al., 2003). The TLKs, TLK1 and TLK2, are conserved Ser-Thr kinases that are critical for regulation of ASF1A and ASF1B, histone H3/H4 chaperones with key roles in histone deposition during DNA replication, DNA repair, and transcription (Carrera et al., 2003; Han et al., 2003; Pilyugin et al., 2009; Roe et al., 1993; Silljé and Nigg, 2001; Silljé et al., 1999). Depletion of both ASF1A and ASF1B results in replication fork arrest in the absence of ssDNA generation or RS signaling, even in cells treated with the ribonucleotide reductase inhibitor hydroxyurea (HU), which normally induces high levels of RS (Groth et al., 2007).

Depletion of total ASF1 induces features of alternative lengthening of telomeres (ALT), a telomerase-independent, recombination-based telomere maintenance mechanism used in 10%–15% of tumors (Hoang and O'Sullivan, 2020; O'Sullivan et al., 2014). ALT+ tumors are frequently characterized by inactivation of the Alpha thalassemia/mental retardation syndrome X-linked (ATRX)-Death-domain associated protein (DAXX) complex, which controls histone H3.3 deposition and maintenance of pericentromeric and telomeric heterochromatin. ASF1 facilitates H3.3 deposition through the Histone Cell Cycle Regulation Defective Homolog A (HIRA) or Chromatin Assembly Factor 1 (CAF1) chaperones and may compensate for a lack of ATRX-DAXX in ALT+ tumors (Clément et al., 2018; Liang et al., 2020; Lovejoy et al., 2012).





(legend on next page)

In cancer cells, defective chromatin assembly caused by ASF1B depletion limits proliferation, and high ASF1B levels correlate with poor patient outcome in breast cancer (Corpet et al., 2011). Similarly, TLKs are critical for nucleosome assembly during DNA synthesis and replication fork stability, but in contrast to ASF1 depletion, that arrests forks without provoking ssDNA accumulation, TLK loss leads to acute RS, with increased levels of ssDNA and DNA double-strand breaks (DSBs) (Groth et al., 2007; Lee et al., 2018b). Both *TLK1* and *TLK2* are maintained in most cancers and often amplified. In some cases, their increased expression correlates with poor prognosis, suggesting they may be potential cancer targets (Kim et al., 2016; Lee et al., 2018b).

DNA damage inducing chemotherapy elicits an inflammatory response involving the induction and secretion of cytokines (Li and Chen, 2018; Rodier et al., 2009). This relies on the detection of cytosolic DNA by Cyclic GMP-AMP Synthase (cGAS) and Stimulator of Interferon Reponse cGAMP Interactor 1 (STING) signaling. Several nuclease activities, including TREX1, SAMHD1, and MRE11, were implicated in suppression of the interferon (IFN) response (Pasero and Vindigni, 2017). SAMHD1 localizes to replication forks where it recruits the MRE11 nuclease to regulate replication fork progression and prevent IFN activation in response to RS (Coquel et al., 2018). In addition to the so-far poorly defined substrates generated at replication forks, both micronuclei—which can result from RS—and extra-chromosomal telomeric repeats (ECTRs) that are produced in ALT+ cancer cells—such as partially single-stranded C-rich telomeric circles (C-circles)—are inducers of cGAS-STING signaling (Chen et al., 2017; Harding et al., 2017; Mackenzie et al., 2017).

We previously demonstrated that TLK depletion impaired *de novo* histone deposition and led to RS (Lee et al., 2018b). To understand the genome-wide impact of TLK depletion, we conducted the Assay for Transposase-Accessible Chromatin using sequencing (ATAC-seq) and RNA sequencing (RNA-seq) to examine chromatin accessibility and transcription. We found that TLK loss increased chromatin accessibility at heterochro-

matic regions and caused spurious transcription of silenced repetitive elements and telomeres. In ALT+ U-2-OS cells and in ALT– HeLa LT cells, TLK depletion hyperactivated or induced hallmarks of ALT, respectively, and robustly activated cGAS-STING-TBK1-mediated innate immune responses. Innate immune responses were attenuated by limiting the production of ECTRs but not by modulating RS signaling. Finally, we show that *TLK2* expression correlates with CIN and anti-correlates with innate and adaptive immune responses in many human tumors, suggesting that high TLK levels may prevent innate immune responses induced by CIN and ALT, thus limiting immune recognition in cancer.

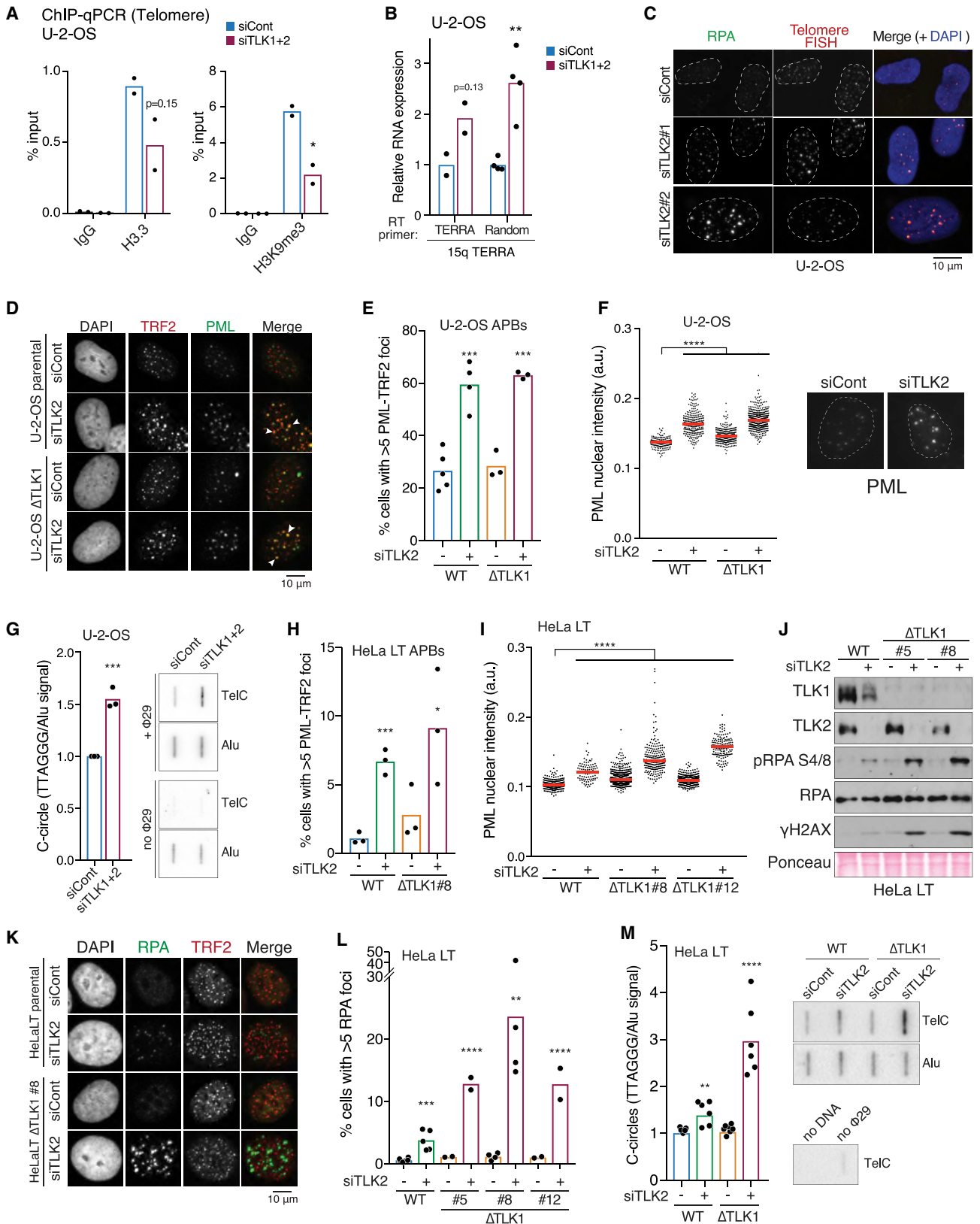
RESULTS

Loss of TLK Activity Compromises Heterochromatin Maintenance

Given that TLK depletion reduced *de novo* histone deposition and provoked RS (Lee et al., 2018b), we sought to determine if particular genomic regions may be hypersensitive to TLK1/2 depletion. To map genome-wide effects of TLK depletion on chromatin accessibility, we used the ATAC (Buenrostro et al., 2013) followed by deep sequencing (ATAC-seq) or quantitative real-time PCR (ATAC-qPCR). We evaluated chromatin accessibility in U-2-OS, following depletion of TLK1, TLK2, or both TLK1 and TLK2. To identify relative chromatin accessibility changes, we considered consensus peaks as those present in at least one of four biological conditions (Figure 1A). From consensus peaks covering the annotated genome, 10% of the genome exhibited differential accessibility upon TLK1/2 depletion (Figure 1B). These significant changes involved regions depleted of accessible peaks (negative fold change [FC]); mainly promoter-transcriptional start site (TSS) regions; and regions enriched with accessible peaks (positive FC), which were mainly intronic and intergenic (Figures 1B, 1C, and S1A–S1C). Single depletion of TLK1 or TLK2 caused similar trends, but differences were more evident following depletion of both (Figure S1B).

Figure 1. Loss of TLK Activity Compromises Heterochromatin Maintenance

- (A) Schematic depicting experimental design of ATAC experiments in U-2-OS.
 (B) Chromatin accessibility changes in U-2-OS upon TLK depletion are statistically significant in 10% of the genome ($n = 2$) (left panel). Genome annotation of peaks with statistically significant negative (2559 peaks) or positive (2941 peaks) FC upon TLK depletion (right panel). See Tables S1 and S2 for additional information.
 (C) Representative Integrative Genomics Viewer (IGV) tracks of ATAC-seq reads of an intronic region (top panel) and intergenic region (bottom panel) that become more accessible upon TLK loss.
 (D) Boxplots of ATAC-seq FC (siTLK1+2 relative to siCont) through different ChromHMM states.
 (E) Boxplots of ATAC-seq FC relative to siCont computed in regions that do or do not overlap with H3K9me3 chromatin immunoprecipitation sequencing (ChIP-seq) (GEO: GSM788078).
 (F) Heatmap of the correlation relationship grouped using hierarchical clustering between ATAC-seq FC (relative to siCont) and large-scale chromatin features at 10-kb resolution.
 (G) ATAC-qPCR analysis of open chromatin at selected genomic regions in U-2-OS. Data of quantitative real-time PCR amplification are normalized to RNA Pol II promoter region and represented relative to the signal obtained in siCont, which was set to 1 ($n = 2$).
 (H) Representative IF images of HP1 α staining in U-2-OS (left panel). High-throughput microscopy (HTM) quantification of chromatin-bound HP1 α levels (right panel). Data are from one biological replicate with $n > 300$ nuclei analyzed and are representative of three biological replicates. Median is shown in red.
 (I) Schematic depicting experimental design of ATAC experiments in HeLa LT.
 (J) Genome annotation of peaks with statistically significant negative (586 peaks for siCont, 70 peaks for siTLK2) or positive (105 peaks for siCont, 137 peaks for siTLK2) FC upon TLK1/2 loss ($n = 2$).
 (K) ATAC-qPCR at selected genomic regions in HeLa LT as in (G) ($n = 2$).
 (L) Boxplots depicting ATAC-seq FC relative to siCont computed in regions that do or do not overlap with H3K9me3 ChIP-seq (GEO: GSM788078).
 **** $p < 0.0001$, *** $p < 0.001$, ** $p < 0.01$, * $p < 0.05$; unpaired t test with Welch's correction (H), unpaired t test (G and K).



(legend on next page)

We focused further analysis on regions that became more accessible, as this could reflect defective chromatin assembly (Figure 1C). To evaluate how accessibility changes correlated with genomic and epigenomic features, we correlated our FCs with chromatin states using the ChromHMM tool (Ernst and Kellis, 2012) and observed heterochromatin (constitutive heterochromatin defined as repetitive/copy number variation [CNV]) had the most prominent increase in accessibility upon TLK1/2 loss (Figure 1D). Consistently, ATAC peaks overlapping with H3K9me3, a heterochromatin marker, were enriched upon TLK1/2 depletion (Figure 1E). At a 10-kb resolution, increased accessibility in TLK1/2-depleted cells positively correlated with H3K9me3 and negatively correlated with the euchromatin mark H3K36me3 and early replication timing (Figures 1F and S1D). At this resolution, we did not observe any correlation with chromosomal locations, including distance to telomeres or centromeres (Figure 1F). Validation by ATAC-qPCR of some high-FC heterochromatic peaks (hit 1 to hit 3), as well as telomeres, confirmed increased accessibility upon TLK loss (Figures 1C and 1G). This was phenocopied by ASF1 depletion, pointing to defective chromatin assembly as the underlying cause (Figure S1E). To determine if TLK1/2 depletion had a general impact on heterochromatin maintenance, we examined chromatin-bound HP1 α , a marker of pericentric heterochromatin, and observed a strong reduction in HP1 α signal following TLK depletion (Figures 1H and S1F).

As U-2-OS cells are ALT+ and lack ATRX, we considered that they could be more dependent upon TLK-ASF1 for H3.3 deposition required for heterochromatin maintenance (Figures 1H and S1F) (Udugama et al., 2015). We evaluated chromatin accessibility in HeLa long telomere (LT) cells, a clone of HeLa 1.2.11 derived with LTs of about 20 kb (Figure 1I) (O'Sullivan et al., 2014) and found that while only 1%–3% of consensus peaks displayed statistical significance, the genomic annotation pattern of peaks enriched or depleted upon TLK loss was very similar to U-

2-OS (Figures 1J and S1G). We validated hit regions and telomeres by ATAC-qPCR in HeLa LT cells (Figures 1K and S1H) and noted that ATAC peaks overlapping with H3K9me3 marks were enriched in Δ TLK1 siTLK2 samples (Figure 1L). Overall, these results revealed that constitutive heterochromatin, which is restricted mainly to gene-poor regions, pericentromeres, and telomeres, is most dependent on TLK activity for maintenance. Moreover, our findings imply that ALT+ U-2-OS cells, lacking ATRX, may be particularly dependent on TLK activity for chromatin maintenance.

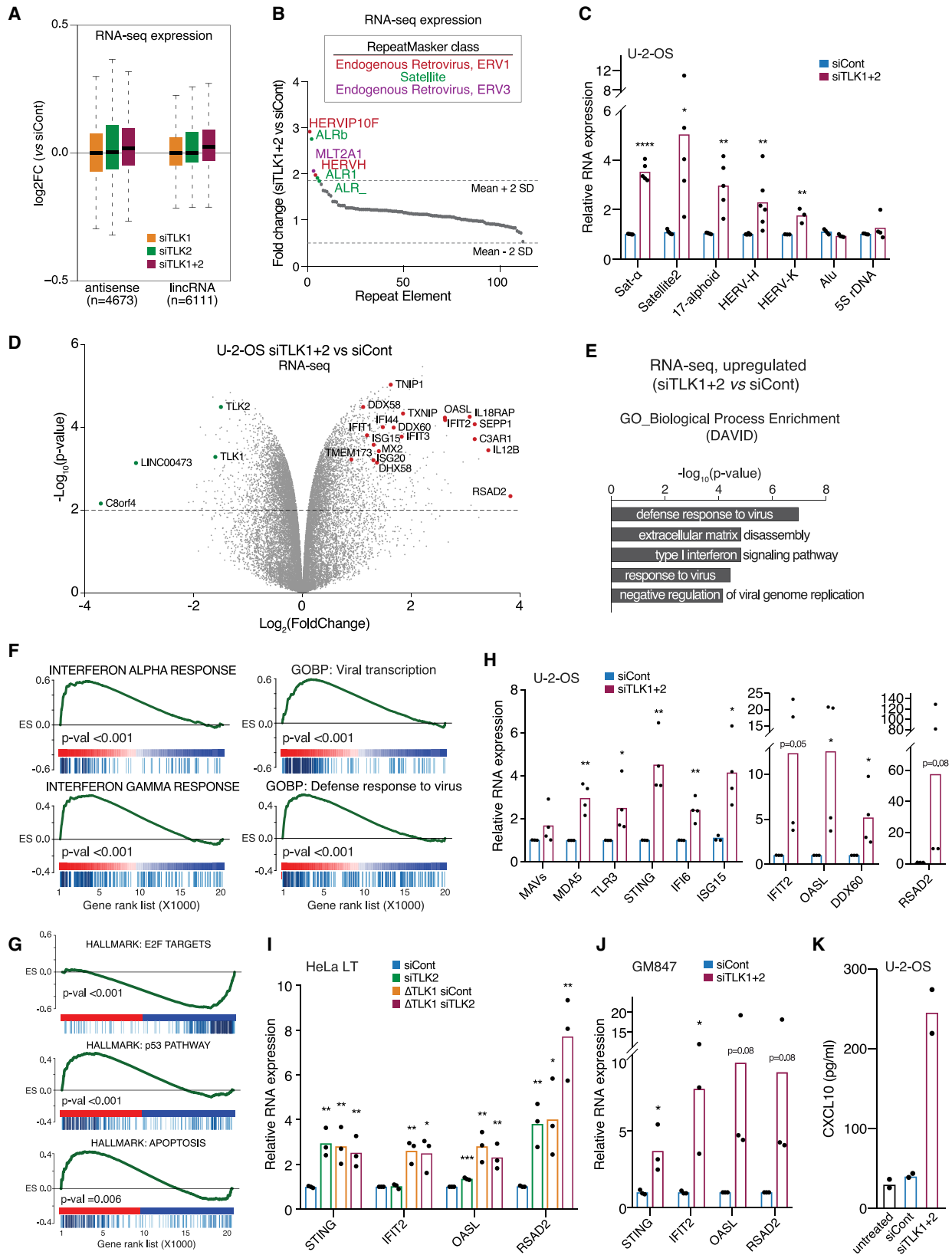
TLK Activity Suppresses Telomeric Recombination

ALT telomeres in *ATRX*^{-/-} cells are characterized by a reduced occupancy of H3.3-containing nucleosomes (Goldberg et al., 2010; Li et al., 2019). H3.3 is required for establishing H3K9me3 and heterochromatin formation, and its absence generates DNA damage and increases telomeric sister chromatid exchange in mouse embryonic stem cells (Udugama et al., 2015). Consistent with a decrease in *de novo* histone deposition in TLK-depleted cells (Lee et al., 2018b), occupancy of H3.3 was reduced in most genomic locations (Figures S2A and S2B). In the absence of TLKs, H3.3 and H3K9me3 occupancy was decreased at telomeres, and transcription of telomeric repeat-containing RNA (TERRA) was elevated (Figures 2A and 2B), suggestive of potential hyper-recombination at these sites.

We further investigated the relationship between RS signaling and telomeres in U-2-OS cells. Nearly all Replication protein A (RPA) accumulated in discrete foci co-staining with the shelterin subunit TRF2 or telomeric fluorescence *in situ* hybridization (FISH) signal upon TLK depletion (Figures 2C and S2C). Increased RPA accumulation at telomeres suggested exposure of telomeric ssDNA. TLK2 or total TLK depletion in U-2-OS cells caused increased numbers of ALT-associated Promyelocytic Leukemia (PML) bodies (APBs), membrane-free compartments that co-stain with TRF2 and PML where ALT-dependent

Figure 2. TLK Activity Suppresses Telomeric Recombination

- (A) ChIP-qPCR analysis of H3.3 and H3K9me3 occupancy at telomeres in U-2-OS. Data of quantitative real-time PCR amplification are normalized to input (n = 2). ChIP-seq data are provided in Table S3.
- (B) Expression of 15q TERRA by quantitative real-time PCR in U-2-OS normalized to B-actin expression levels. The signal obtained in siCont was set to 1 (n = 2 for RT primer "TERRA," n = 4 for RT primer "Random").
- (C) IF-FISH staining of chromatin-bound RPA and telomeres in U-2-OS.
- (D) Representative IF of APBs in U-2-OS. White arrowheads indicate TRF2-PML co-localization.
- (E) APB quantification in U-2-OS scored as cells with more than five TRF2-PML colocalizing foci, with >100 cells scored per individual experiment (n = 5 for siCont, n = 4 for siTLK2, n = 3 for Δ TLK1 siCont/siTLK2).
- (F) HTM quantification of chromatin-bound PML nuclear intensity in U-2-OS. Data are from one biological replicate with n >180 nuclei analyzed and are representative of four biological replicates. Representative images are shown. Median is shown in red.
- (G) Quantification of telomeric C-circles in U-2-OS 48 h after siRNA treatment. Telomeric signal was normalized by Alu signal (n = 3). Representative slot blot is shown in the right panel.
- (H) APB quantification in HeLa LT, scored as in (E), with >100 cells scored per individual experiment (n = 3).
- (I) HTM quantification of chromatin-bound PML nuclear intensity in HeLa LT. Data are from one biological replicate with >100 nuclei analyzed and are representative of three biological replicates. Median is shown in red.
- (J) Western blot of RS and DDR signaling markers upon TLK2 depletion in HeLa LT WT and Δ TLK1.
- (K) Representative IF of RPA-TRF2 staining in HeLa LT.
- (L) Quantification of cells with more than five RPA discrete foci, with >200 cells evaluated per individual experiment (n = 6 siCont, n = 5 siTLK2, n = 2 Δ TLK1#5 and Δ TLK1#12, n = 4 Δ TLK1#8).
- (M) Quantification of telomeric C-circles in HeLa LT WT or Δ TLK1 72 h after siRNA treatment. Telomeric signal was normalized by Alu signal (n = 7 siCont, n = 6 siTLK2). Representative slot blot shown in the right panel.
- ****p < 0.0001, ***p < 0.001, **p < 0.01, *p < 0.05; unpaired t test with Welch's correction (F and I), unpaired t test, one-tailed (G and M).



(legend on next page)

telomere recombination takes place (Figures 2D, 2E, and S2D) (Hoang and O'Sullivan, 2020). Additionally, a remarkable increase in PML body intensity suggested ALT-associated telomere clustering (Figure 2F) (Draskovic et al., 2009). TLK depletion resulted in a mild but significant increase in C-circles in ALT+ U-2-OS cells, which already generate large numbers of C-circles (Figure 2G) (Henson et al., 2009, 2017).

Since ASF1 depletion induces ALT features in ALT- cell lines (O'Sullivan et al., 2014), we examined TLK depletion in HeLa LT cells, which elongate telomeres via telomerase. Total TLK depletion, achieved by TLK2 siRNA in TLK1 knockout clones (Δ TLK1), increased APBs and the intensity of PML bodies (Figures 2H and 2I). Total TLK loss caused RS and DSBs in these cells, visualized by phosphorylation of RPA at S4/8 and γ H2AX (Figure 2J) and accumulation of chromatin-bound RPA that often co-localized with telomeres (Figures 2K, 2L, and S2E). To assess recombination at ALT- telomeres, we quantified C-circles and observed a significant increase following loss of both TLKs (Figure 2M). Together, these data demonstrate that despite causing a RS phenotype not observed with ASF1 depletion, TLK loss phenocopies ASF1 depletion by compromising telomeric chromatin maintenance and inducing features of the ALT pathway.

TLK Depletion Activates Innate Immune Signaling

Aside from telomeres, disruption of heterochromatin by TLK depletion could also affect the silencing of other genomic loci. To address this, we performed RNA-seq with rRNA depletion in U-2-OS so we could analyze mRNA and other RNA species devoid of a poly(A) tail. We analyzed differential RNA expression by aligning to GENCODE-annotated genetic variants (Harrow et al., 2012), including protein-coding loci with alternatively spliced variants, noncoding loci, and pseudogenes. From the GENCODE categories, TLK depletion significantly upregulated the expression of antisense RNA and long intergenic noncoding RNA (lincRNA) (Figure 3A), consistent with TLKs suppressing ncRNA transcription. Alignment of the RNA-seq data to Repbase (Bao et al., 2015) revealed a significant increase in the expression of satellite RNAs and some human endogenous retroviruses (HERVs) upon TLK depletion (Figure 3B). ATAC-seq data alignment to Repbase confirmed that chromatin accessibility at these

repetitive elements was significantly increased in TLK-depleted U-2-OS cells, and these changes were less prominent in HeLa LT (Figures S3A and S3B), likely reflecting ATRX-DAXX status. Using quantitative real-time PCR, we validated the increased expression of several repetitive elements upon TLK depletion in U-2-OS, including satellites and HERVs, whereas other repetitive elements, such as 5S rDNA or Alu, remained unaffected (Figure 3C).

Analysis of differential gene expression ($-\text{Log}_2\text{FC}$ cut-off of 2) revealed that upon TLK loss, more genes were upregulated than downregulated (Figure 3D), with the strongest change being an innate immune response comprising type-I IFN and tumor necrosis factor alpha (TNF- α) programs. Gene Ontology (GO) analysis confirmed that antiviral responses were the most enriched categories in the upregulated genes (Figure 3E), and gene set enrichment analysis (GSEA) uncovered that upregulation of IFN response signatures was highly significant in TLK-depleted cells (Figure 3F). In addition, checkpoint response and apoptosis signatures were upregulated, whereas the E2F target signature was downregulated (Figure 3G), corroborating p53 activation, G1/S cell cycle arrest, and cell death phenotypes previously reported (Lee et al., 2018b). We further validated upregulation of IFN response genes by quantitative real-time PCR in U-2-OS cells and in two additional cell lines, ALT+ GM847 and ALT- HeLa LT (Figures 3H–3J, S3C, and S3D). Notably, numerous genes that recognize viral RNAs were upregulated, including *MDA5/IFIH1*, *RIG-I/DDX58*, and *TLR3*, as well as *STING/TMEM173*, an important mediator in response to cytosolic DNA detected by cGAS. These were accompanied by a number of other IFN-stimulated genes, including *IFI6*, *ISG15*, *IFIT2*, *OASL*, *DDX60*, *CXCL10*, and *RSAD2* (Figures 3H–3J). To assess whether the transcriptional induction of innate immune genes resulted in pro-inflammatory cytokine secretion, we measured CXCL10/IP-10 protein in the cellular supernatant by ELISA and found increased levels upon TLK depletion (Figure 3K).

Innate Immune Activation Is Dependent on the cGAS-STING-TBK1 Axis

RS, ERVs, and ECTRs have all been implicated in innate immune activation. We next examined the molecular trigger for

Figure 3. TLK Depletion Activates Innate Immune Signaling

- (A) Boxplots of RNA-seq noncoding expression, such as antisense RNA or lincRNA, relative to siCont (n = 2).
 (B) Analysis of repetitive RNA expression (RNA-seq, n = 2). FC in RNAs (siTLK1+2 versus siCont) transcribed from different repeat types was ranked from highest to lowest. Horizontal dotted line represents a cut-off of 2 SD from the mean. Repeats enriched more than 2 SD from the mean are labeled, and colors represent the RepeatMasker broad repeat class to which that repeat type belongs.
 (C) Expression of DNA repetitive elements by quantitative real-time PCR in U-2-OS. Data are normalized to B-actin, and expression in siCont conditions was set to 1 (n = 5 Sat- α /Satellite2/17-alphoid, n = 6 HERV-H, n = 3 HERV-K, n = 4 Alu/5S rDNA).
 (D) Volcano plot representing gene expression profile of siTLK1+2 versus siCont obtained from RNA-seq in U-2-OS (n = 2). Gray dots indicate genes, and green dots represent the most downregulated genes together with TLK1 and TLK2. Red dots represent genes belonging to the IFN response. The p values and FC are computed by fitting a linear model with the R package limma. See Tables S4 and S5 for additional data.
 (E) GO analysis (enrichment biological process) of RNA-seq differentially upregulated genes upon TLK1/2 knockdown.
 (F) GSEA of RNA-seq positively enriched genes related to innate immunity corresponding to the samples siTLK1+2 versus siCont.
 (G) GSEA plots of selected differentially expressed gene categories corresponding to the RNA-seq samples siTLK1+2 versus siCont.
 (H) Validation of expression levels of RNA and DNA sensors and IFN response genes by quantitative real-time PCR in U-2-OS. Data analyzed as in (C) (n = 4).
 (I) Expression levels of IFN response genes by quantitative real-time PCR in HeLa LT. Data were analyzed as in (C) (n = 3).
 (J) Expression levels of IFN response genes by quantitative real-time PCR in GM847. Data were analyzed as in (C) (n = 3).
 (K) CXCL10 concentration was measured in the supernatant of U-2-OS 96 h after siRNA treatment by ELISA (n = 2).

****p < 0.0001, ***p < 0.001, **p < 0.01, *p < 0.05; unpaired t test, one-tailed (C and H–J).

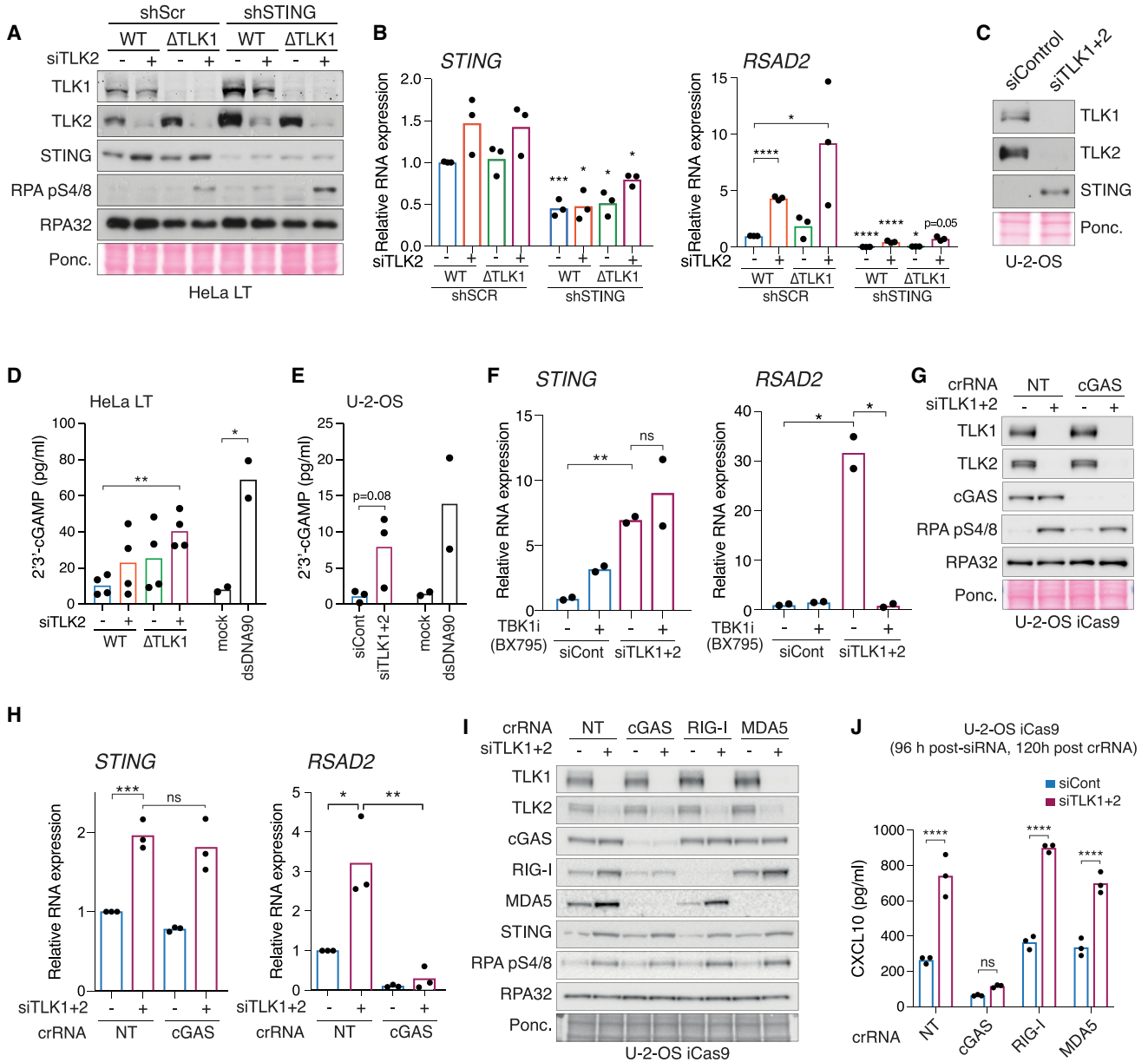


Figure 4. Innate Immune Activation Is Dependent on the cGAS-STING-TBK1 Axis

(A) Western blot of HeLa LT infected with scramble shRNA or shRNA against STING, 48 h after siRNA treatment.

(B) Expression levels of *STING* and *RSAD2* by quantitative real-time PCR in HeLa LT 48 h after siRNA treatment. Data are normalized to B-actin and siCont signal set to 1 (n = 3).

(C) Western blot of STING in U-2-OS cells, 48 h after siRNA treatment.

(D) 2'3'-cGAMP production ELISA analysis in HeLa LT 72 h after siRNA treatment. Transfection with dsDNA90 24 h prior to harvesting is included as a positive control (n = 4 for siRNA, n = 2 for dsDNA90).

(E) 2'3'-cGAMP production analyzed by ELISA in U-2-OS treated as in (D) (n = 3 for siRNA, n = 2 for dsDNA90).

(F) Expression levels of *STING* and *RSAD2* by quantitative real-time PCR in U-2-OS mock treated or treated with 1 μ M BX795 for 24 h. Data analyzed as in (B) (n = 2).

(G) Western blot showing cGAS knockout and TLK depletion in U-2-OS iCas9 cells. Ponceau staining shown as a loading control.

(H) Expression levels of *STING* and *RSAD2* by quantitative real-time PCR in U-2-OS iCas9 72 h after knockout induction and 48 h after siRNA treatment. Data analyzed as in (B) (n = 3).

(I) Western blot showing cGAS/RIG-I/MDA5 knockouts and TLK depletion in U-2-OS iCas9 120 h after knockout induction and 96 h after siRNA treatment. Ponceau staining shown as a loading control.

(J) CXCL10 concentration measured in the supernatant of U-2-OS iCas9 cells by ELISA (n = 3).

****p < 0.0001, ***p < 0.001, **p < 0.01, *p < 0.05; unpaired t test (B, D, and F-H), two-way ANOVA (J).

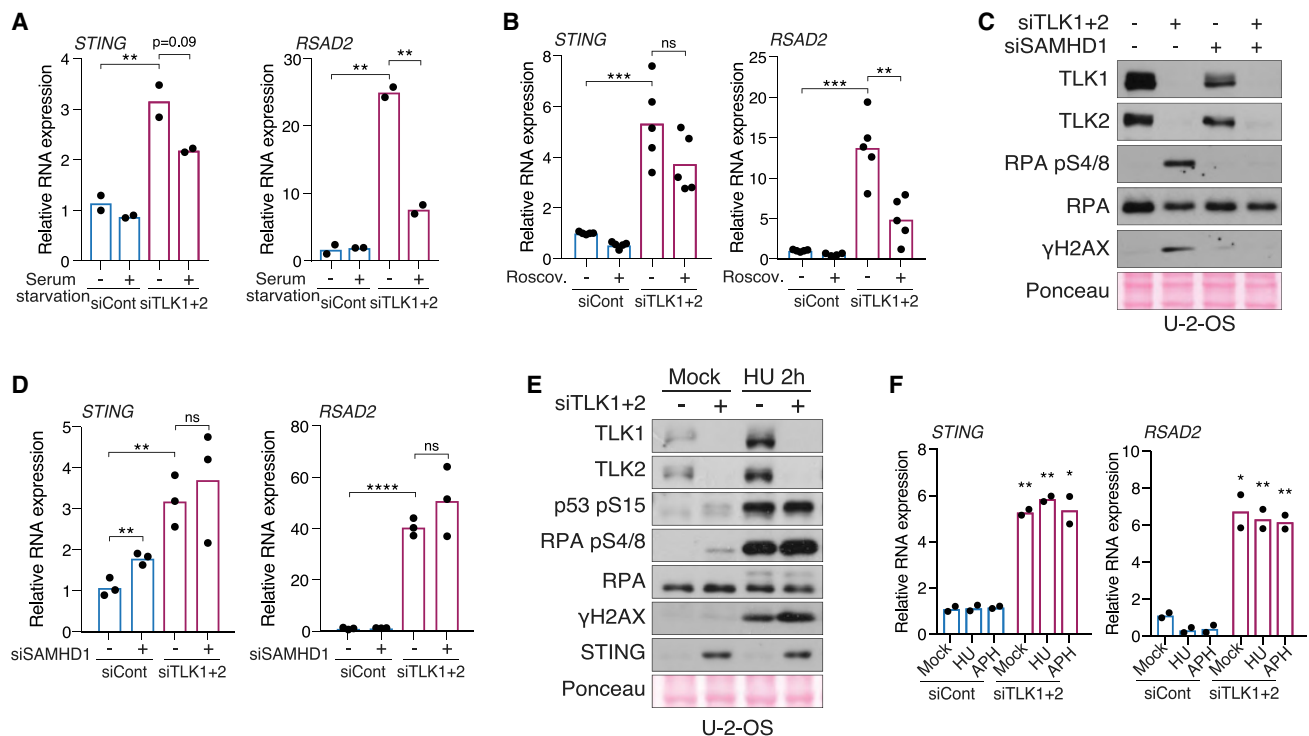


Figure 5. Innate Immune Activation Is Independent of RS

(A) Expression levels of *STING* and *RSAD2* by quantitative real-time PCR in control or serum-starved U-2-OS 48 h after siRNA treatment. Data are normalized to B-actin and siCont expression set to 1 (n = 2).
 (B) Expression levels of *STING* and *RSAD2* by quantitative real-time PCR in U-2-OS mock-treated or treated with 50 μ M Roscovitine for 5 h. Data analyzed as in (A) (n = 5).
 (C) Western blot showing single or double depletion of TLKs and SAMHD1 in U-2-OS harvested 48 h after siRNA treatment. Ponceau staining shown as a loading control.
 (D) Expression levels of *STING* and *RSAD2* by quantitative real-time PCR in U-2-OS 48 h after siRNA treatment. Data analyzed as in (A) (n = 3).
 (E) Western blot in U-2-OS 48 h after siRNA transfection mock-treated or with 2 mM HU for 2 h. Ponceau staining shown as a loading control.
 (F) Expression levels of *STING* and *RSAD2* by quantitative real-time PCR in U-2-OS mock-treated or treated with 0.5 mM HU for 2 h or 0.5 μ M aphidicolin for 4 h. Data analyzed as in (A) (n = 2).
 ****p < 0.0001, ***p < 0.001, **p < 0.01, *p < 0.05; unpaired t test (A, B, D, and F).

upregulation of *RSAD2* and *STING* after TLK depletion. Depletion of STING in HeLa LT cells severely reduced *RSAD2* induction without impacting RS signaling, thus implicating the cGAS-STING pathway (Figures 4A and 4B). Many ALT+ tumor cell lines, including U-2-OS, epigenetically silence STING, presumably to prevent the activation of innate immunity through cGAS sensing of ECTRs (Barroso-González et al., 2019; Chen et al., 2017; Wu et al., 2018; Xia et al., 2016). We observed increased mRNA and protein levels of STING, as well as *RSAD2* induction in ALT+ U-2-OS cells (Figures 3H and 4C). Canonical STING activation induces type-I IFN genes through TBK1 and the transcription factor IRF3, acting primarily in response to production of 2'3'-cGAMP by cGAS, following dsDNA recognition (Chen et al., 2016). Both HeLa LT and U-2-OS cells increased 2'3'-cGAMP production after TLK depletion to a similar extent as controls transfected with a dsDNA90 molecule (Figures 4D and 4E). Treatment of U-2-OS cells with a TBK1 inhibitor (BX795) completely abolished the upregulation of *RSAD2*, but not *STING*, following TLK depletion (Figure 4F). Knockout of cGAS using an inducible Cas9 (iCas9) system in

U-2-OS similarly did not influence *STING* levels but impaired activation of *RSAD2*, *OASL*, and *IFIT2* (Figures 4G, 4H, and S4A). These results suggested that STING reactivation occurred through desilencing, rather than by cGAS-mediated pathways. Consistent with this, increased accessibility of the STING promoter was detected in TLK-depleted U-2-OS cells (Figure S4B).

In addition to cGAS, RIG-I and MDA5, which were both upregulated following TLK depletion (Figures 3D and 3H), sense distinct RNA species that trigger their interactions with Mitochondrial Antiviral Signaling Protein (MAVS) to activate IFN signaling (Zevini et al., 2017). Given the increased transcription of ncRNA observed upon TLK depletion (Figures 3A–3C) and that MAVS and STING interact (Ishikawa and Barber, 2008; Zhong et al., 2008), we examined their influence on *STING* and *RSAD2* induction. Unlike cGAS, neither RIG-I nor MDA5 knockout impaired *RSAD2* activation upon TLK depletion. STING reactivation also occurred regardless of RIG-I or MDA5 status (Figures S4C–S4F), indicating they did not influence the response at either level. Finally, we confirmed that CXCL10 secretion was also dependent on cGAS, but not RIG-I or

MDA5, following TLK depletion (Figures 4I and 4J). Collectively, these data demonstrate that the cGAS-STING-TBK1 pathway promotes innate immune activation in TLK1/2-depleted cells, and STING reactivation occurs independently of the dsDNA sensor cGAS or the RNA sensors RIG-I and MDA5.

Innate Immune Activation Is Independent of RS

We previously demonstrated that H3/H4 deposition was impaired in TLK-depleted cells and strongly dependent upon active DNA replication, when the highest levels of histone exchange occur (Lee et al., 2018b). Similarly, we found that innate immune activation upon TLK loss was strongly reduced following serum starvation or treatment of cells with the CDK2 inhibitor Roscovitine (Figures 5A and 5B). RS has been implicated in innate immune activation, particularly through SAMHD1 promotion of MRE11-mediated resection of stalled forks (Coquel et al., 2018). The depletion of SAMHD1 mitigated RS and DSBs in TLK-depleted U-2-OS cells (Figures 5C and S5A). However, the activation of both *RSAD2* and *STING* was unaffected by SAMHD1 loss following TLK depletion (Figure 5D). Depletion of MRE11 by siRNA or its inhibition with Mirin also attenuated RS signaling (Figures S5A and S5B). This partially alleviated *RSAD2* and, to a lesser extent, *STING*, although impairing MRE11 may have stronger effects on cell cycle progression than SAMHD1 depletion (Figure S5C). Treatment of U-2-OS cells with HU to induce RS did not activate *STING* or *RSAD2* expression per se in various cell lines, with the exception of RPE-1 cells (Figures 5E, 5F, and S5D–S5F). Notably, *STING* protein levels remained low in HU-treated U-2-OS cells (Figure 5E). In addition, *STING* and *RSAD2* activation following TLK depletion were not consistently enhanced by HU or aphidicolin (APH) in U-2-OS or HeLa LT (Figures 5F, S5E, and S5F). While micronuclei were induced 2-fold by TLK depletion, they also did not correlate with RS levels (Figures S5G and S5H). These data indicate that attenuation (SAMHD1 depletion) or enhancement (HU) of RS signaling induced by TLK depletion does not influence innate immune induction. Conversely, cell cycle progression promotes the response, suggesting that replication-coupled histone loss drives innate immune signaling following depletion of TLK1/2.

ALT Contributes to Innate Immune Induction Following TLK Depletion

To determine if ALT could be a major driver of innate immunity in TLK-depleted cells, we examined the influence of the Bloom syndrome protein (BLM) helicase on C-circle production in HeLa LT cells. BLM is required for resection by DNA2/EXO1, as well as for dissolution of ALT recombination intermediates as part of the BLM, TOP3a, RMI1, and RMI2 (BTR) complex (Cejka et al., 2010; Gravel et al., 2008; Nimonkar et al., 2011; Panier et al., 2019; Sobinoff et al., 2017). BLM depletion strongly attenuated C-circles and reduced *STING* and *RSAD2* induction in HeLa LT cells following TLK depletion (Figures 6A, 6B, and S6A). We next examined U-2-OS cells lacking PML, a key component of APBs that is required for efficient C-circle production (Figure 6C) (Loe et al., 2020). Deletion of PML also strongly attenuated *RSAD2* induction following TLK1/2 depletion and reduced extranuclear telomeric FISH signal, indicating that ECTR production contributes to innate immune activation in

TLK-depleted cells (Figures 6D, S6B, and S6C). Notably, TLK depletion mildly upregulated C-circle production in ALT+ U-2-OS, which already produces high levels of C-circles (Figures 2G and 6C), but strongly upregulated *RSAD2* through reactivation of *STING* (Figure 4C). As these results implicated C-circles in innate immune signaling following TLK depletion, we examined the ability of the fusion protein TRF1-FokI, which generates telomeric breaks that undergo break-induced telomere synthesis and produces C-circles in a BLM/PML-independent manner (Cho et al., 2014; Dilley et al., 2016), to induce innate immune signaling in U-2-OS. Expression of TRF1-FokI wild type (WT), but not the nuclease dead (D450A), increased C-circle levels in U-2-OS cells to a similar extent as TLK depletion (Figures 6E and 6F). However, only TLK-depleted cells activated *STING* (Figure 6G), suggesting that epigenetic silencing of *STING* requires TLK-mediated chromatin maintenance to prevent innate immune activation by ECTRs. Together, we found that the production of C-circles following TLK loss triggers the activation of cGAS-STING-TBK1-mediated innate immune responses. Additionally, in cells where *STING* is silenced, a first-tier reactivation at the epigenetic level is required to fully promote this IFN response.

TLK Expression Correlates with Suppressed Innate Immune Signaling in Human Cancer

Tumors with unstable genomes, micronuclei, and ALT+ telomeres generate sources of immunostimulation that can induce an IFN response and often circumvent this pathway by silencing *STING* epigenetically to minimize immune surveillance (Bakhom and Cantley, 2018; Chen et al., 2017; Wu et al., 2018). We next analyzed publicly available datasets from The Cancer Genome Atlas (TCGA) for correlations among *TLK1* and *TLK2* levels, chromosomal instability, and immunity across different tumor types. Expression levels of *TLK1* and *TLK2* anti-correlated significantly with *STING* (encoded by the *TMEM173* gene) in many tumor types (Figures 7A and 7B). We reasoned that tumors with high levels of genome instability may select for *STING* silencing and higher levels of TLK activity to suppress toxic RS. We examined CIN levels in tumors by using a previously defined signature containing a 25-gene set (Carter et al., 2006), as well as the aneuploidy score estimated from comparative genomic hybridization (CGH) SNP arrays, a measure independent of gene expression (Taylor et al., 2018). While *TLK1* expression levels only positively correlated with CIN/aneuploidy levels in selected tumor types, *TLK2* expression significantly correlated with CIN/aneuploidy levels in most tumor types (Figure 7B).

Following these correlations, we next addressed whether $TLK2^{\text{high}}\text{-}STING^{\text{low}}\text{-}CIN^{\text{high}}$ tumors were differentially infiltrated by immune cell populations. We took measurements of leukocyte and stromal fractions based on methylation and expression signatures (Taylor et al., 2018) and detected several tumor types with significantly reduced fractions of immune infiltration correlating with high TLK expression (Figure 7B). Interestingly, some of the tumor types with this behavior are described to be immune infiltration depleted or “cold” tumors such as low-grade glioma (LGG), adrenocortical carcinoma (ACC), liver hepatocellular carcinoma (LIHC), glioblastoma multiforme (GBM), and sarcoma (SARC) (Figure 7B) (Thorsson et al., 2018), and several of these

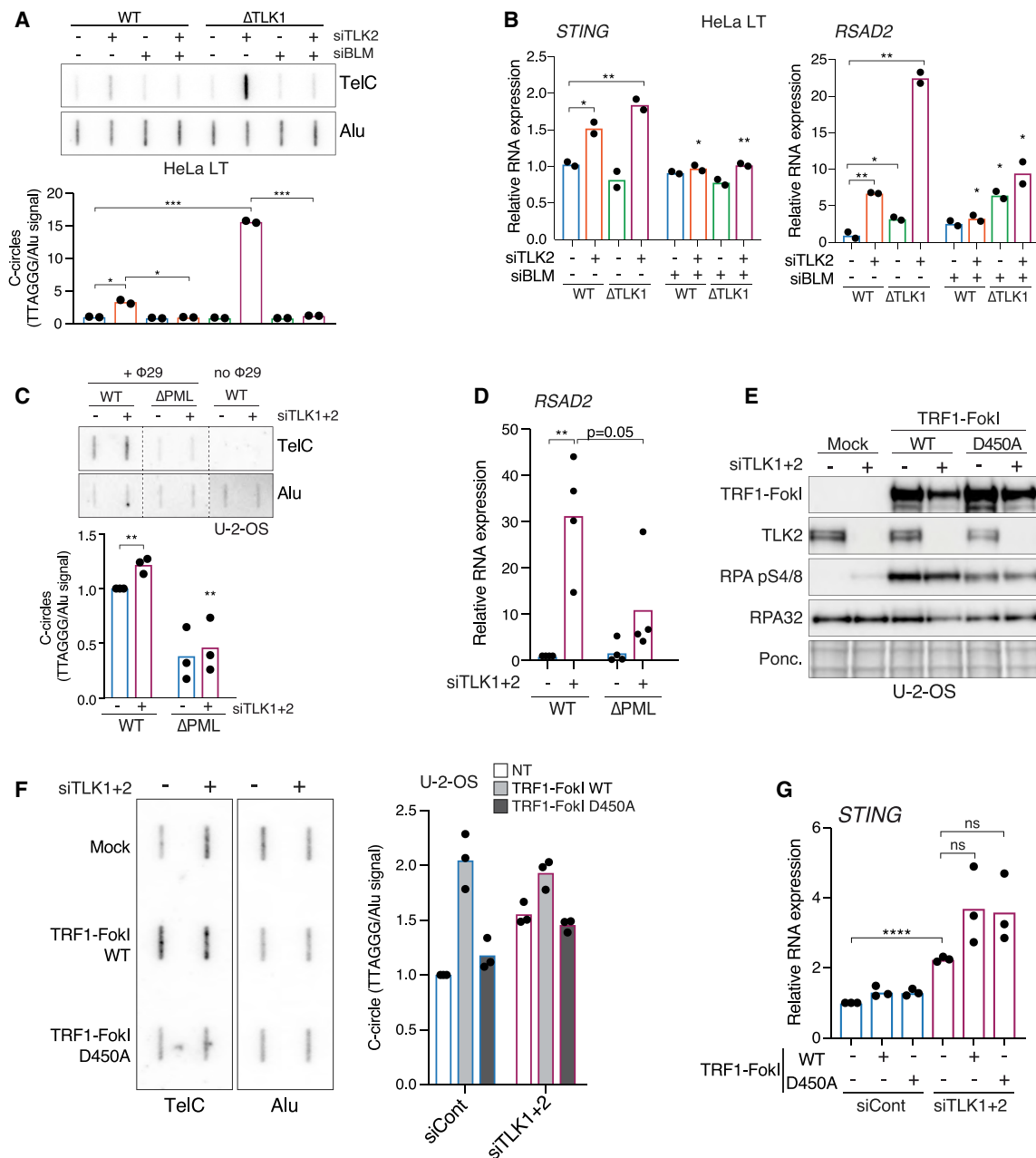


Figure 6. ALT Induction Contributes to Innate Immunity Following TLK1/2 Depletion

(A) Telomeric C-circle quantification in HeLa LT. TelC signal was normalized by Alu signal (n = 2). Representative slot blot shown in top panel.
 (B) Expression levels of *STING* and *RSAD2* by quantitative real-time PCR in HeLa LT cells 48 h after treatment with corresponding siRNAs. Data are normalized to B-actin and siCont expression set to 1 (n = 2).
 (C) Telomeric C-circle quantification in U-2-OS. TelC signal was normalized by Alu signal (n = 3). Representative slot blot shown in top panel.
 (D) Expression levels of *RSAD2* by quantitative real-time PCR in U-2-OS 48 h after siRNA treatment. Data analyzed as in (B) (n = 4).
 (E) Western blot showing TLK depletion and TRF1-FokI expression in U-2-OS 48 h after siRNA and 24 h after TRF1-FokI transfection. Ponceau staining shown as a loading control.
 (F) Telomeric C-circle quantification in U-2-OS expressing TRF1-FokI. TelC signal was normalized by Alu signal (n = 3). Representative slot blot shown in left panel.
 (G) Expression levels of *STING* by quantitative real-time PCR in U-2-OS cells treated as in (E). Data analyzed as in (B) (n = 3).
 ****p < 0.0001, ***p < 0.001, **p < 0.01, *p < 0.05; unpaired t test (A–D and G).

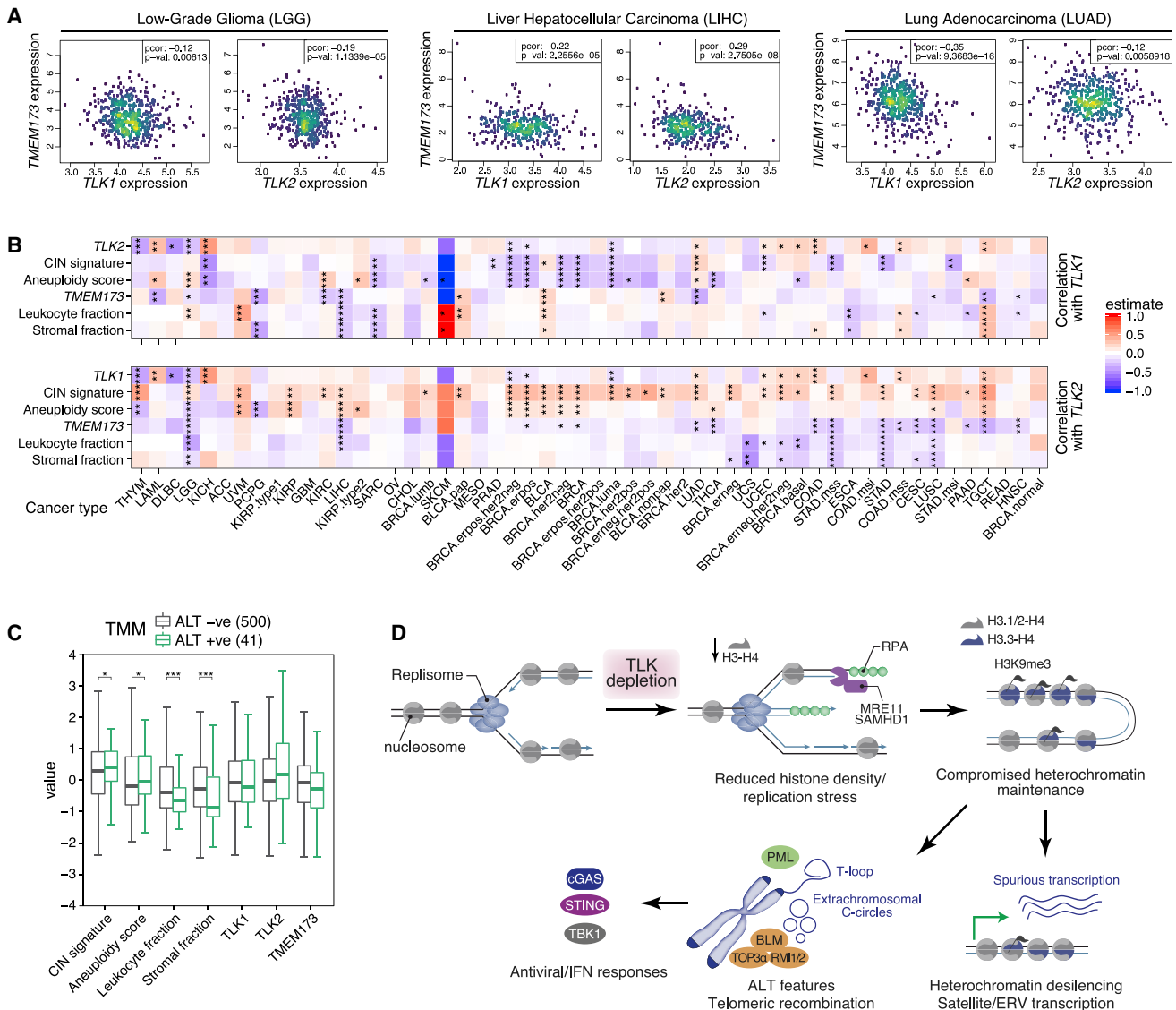


Figure 7. TLK Expression Correlates with Suppressed Innate Immune Signaling in Human Cancer

(A) Correlation between *TLK1/TLK2* and *STING* (*TMEM173*) in the TCGA datasets of low-grade glioma (LGG), liver hepatocellular carcinoma (LIHC), and lung adenocarcinoma (LUAD).

(B) Heatmaps with correlations of expression levels of *TLK1* and *TLK2* with CIN signature, aneuploidy score, *STING* (*TMEM173*), and signatures of tumor-immune populations across different TCGA datasets. Stars indicate adjusted p values for multiple comparisons using Benjamini-Hochberg (***) $p < 0.001$, ** $p < 0.01$, * $p < 0.05$.

(C) Boxplot of expression levels of genes, CIN signature, aneuploidy score, and different signatures of tumor-immune populations. Analysis was performed in different merged TCGA datasets where TMM status was defined. Stars indicate adjusted p values for multiple comparisons using Benjamini-Hochberg (***) $p < 0.001$, ** $p < 0.01$, * $p < 0.05$.

(D) Model of how TLK activity maintains heterochromatin state and its loss promotes spurious transcription and telomere recombination, triggering an innate immune response.

tumor types are frequently ALT+ (Ceccarelli et al., 2016; Lee et al., 2018a). Lastly, we analyzed the relationship between different telomere maintenance mechanisms (TMMs) and the signatures described above. Overall, ALT+ tumors positively correlated with CIN/aneuploidy levels and anti-correlated with signatures of immune infiltration (Figure 7C). Despite not being significant, potentially due to variability across cancer types

and a low number of annotated ALT+ tumors in any given cohort, ALT+ tumors showed a tendency toward higher levels of *TLK2* and lower levels of *STING*. This suggests that tumors that harbor high levels of genome instability (CIN^{high} or ALT+ tumors) may select for high TLK levels and defective cytosolic DNA sensing by *STING* silencing, as a means to prevent tumor recognition by the immune system.

DISCUSSION

Here, we establish that TLKs play a critical role in chromatin maintenance and, if compromised, result in the induction of a cGAS-STING-TBK1-dependent IFN response, even in cells where STING was epigenetically silenced. TLKs promote heterochromatin maintenance at repetitive genome elements and telomeres, and their depletion results in epigenome instability characterized by spurious transcription of ERVs and ncRNAs and enhanced features of ALT (Figure 7D). This innate immune response is augmented by DNA replication, reflecting the fact that TLK depletion phenotypes entail passage through S-phase where histone exchange levels are highest, but is not influenced by the intensity of RS signaling *per se*. The induction of the IFN response in TLK-depleted ALT+ cells is first dependent on STING reactivation and then on stimulation of the pathway through ECTRs generated in a BTR-PML-dependent manner. However, we cannot exclude a potential contribution of RS, micronuclei, ERVs, or reverse-transcribed transcripts to the IFN response (Coquel et al., 2018; De Cecco et al., 2019; Gasser et al., 2005; Heijink et al., 2019; Reisländer et al., 2019). Collectively, our results indicate that faulty heterochromatin maintenance and elevated telomeric recombination in TLK-depleted cells lead to the induction of innate immunity.

Activation of cGAS-STING by DNA damage and RS, particularly through the recognition of micronuclei, is well documented (Harding et al., 2017; Kreienkamp et al., 2018; Mackenzie et al., 2017). By-products of replication fork processing have been implicated in innate immunity by SAMHD1-MRE11-suppressing IFN response activation following treatment with HU (Coquel et al., 2018). We identified a clear separation of function, as SAMHD1 is required for RS signaling but dispensable for innate immune activation following TLK depletion (Figures 5C and 5D). Elevated RS signaling by HU treatment failed to trigger or increase the IFN response in WT or TLK-depleted cells, suggesting it is not the primary cause. Perturbation of the epigenetic landscape by depleting H3.3, multiple H1 genes, or DNA methylases resulted in transcription of noncoding repeat elements from heterochromatin, similar to what we have observed here following TLK depletion, and this was accompanied by the activation of an antiviral response in some cases (Chiappinelli et al., 2015; Elsäasser et al., 2015; Izquierdo-Bouldstridge et al., 2017). This is the first association of TLK activity with the silencing of endogenous viruses and innate immunity, although TLK2 was identified in a screen for gammaherpesvirus latency, a process that involves both epigenetic mechanisms and interactions with innate immune signaling (Dillon et al., 2013; Steed et al., 2007).

ALT+ cells are typically characterized by high levels of CIN and higher basal levels of RS, and they display complex karyotypes (Gagos et al., 2008; Marzec et al., 2015). In addition, ECTRs generated by ALT induce the cGAS-STING pathway and were proposed to provide selective pressure for the epigenetic silencing of STING to suppress potentially cytostatic innate immune signaling (Chen et al., 2017). ALT+ cells deficient in ATRX may also have a higher dependency on ASF1 and, thus, TLK activity, to support H3.3 deposition and heterochromatin maintenance (Liang et al., 2020; Lovejoy et al., 2012). This is consistent with previous work that showed redundancy in the

histone chaperone network that can mitigate deleterious effects arising upon histone pool or histone chaperone imbalances (Drané et al., 2010; Lacoste et al., 2014). Although TLK activity suppresses ALT, TLK dysfunction is unlikely to be an ALT driver event in cancer, since both *TLK1* and *TLK2* are very rarely mutated or deleted in cancer genomes and are required for DNA replication (Lee et al., 2018b). Instead, ALT+ cells may be addicted to and select for TLK activity in order to support heterochromatin maintenance in the absence of ATRX and circumvent innate immune responses.

Our results suggest that reactivation of STING expression in ALT+ cancer cells upon TLK inhibition would be a potential strategy to re-sensitize ALT+ or CIN cells to cytosolic DNA fragments. This inflammatory response may render cancer cells vulnerable to cytotoxic immune cell recruitment and enhance immunotherapy approaches. This is supported by a recent *in vivo* CRISPR/Cas9 screen where ASF1A deletion enhanced the efficacy of PD-1 immunotherapy (Li et al., 2020), as well as by the use of inhibitors for key regulators of epigenome maintenance, CDK9 and DNMT1 (Zhang et al., 2018), and STING agonists as stand-alone agents or in enhancing the effects of immunotherapy (Benci et al., 2016; Curran et al., 2016; Ramanjulu et al., 2018). However, IFN responses have also been implicated in promoting metastasis in CIN^{high} tumors, and it is likely that important context-dependent effects of agents that activate STING will need to be considered (Bakhoum et al., 2018).

Taken together, we have uncovered a complex connection among TLK-mediated chromatin maintenance, ALT, and the innate immune response. These results suggest that TLK activity may promote immune suppression in a subset of tumors, and its inhibition could therefore represent a novel rational targeted therapy to render ALT+ or CIN^{high} cancers more vulnerable to the induction of cell death and enhance existing therapies. Moreover, the newly uncovered role of TLK activity in the suppression of innate immunity may be highly relevant to the etiology of intellectual disability/autism spectrum disorder in patients with germline *TLK2* mutations (Lelieveld et al., 2016; Novellino et al., 2020; Reijnders et al., 2018; Segura-Bayona and Stracker, 2019).

STAR★METHODS

Detailed methods are provided in the online version of this paper and include the following:

- KEY RESOURCES TABLE
- RESOURCE AVAILABILITY
 - Lead Contact
 - Materials Availability
 - Data and Code Availability
- EXPERIMENTAL MODEL AND SUBJECT DETAILS
 - Cell lines
- METHOD DETAILS
 - Drug treatments
 - siRNA/crRNA transfections
 - Western blot analysis
 - Cytokine Detection
 - 2'3'-cGAMP ELISA
 - Immunofluorescence (IF) and IF-FISH

- RNA isolation and RT-qPCR
- ATAC-seq and -qPCR
- Chromatin immunoprecipitation (ChIP)
- RNA-seq
- C-circle assay
- Analysis of TCGA signatures

● **QUANTIFICATION AND STATISTICAL ANALYSIS**

SUPPLEMENTAL INFORMATION

Supplemental Information can be found online at <https://doi.org/10.1016/j.celrep.2020.107983>.

ACKNOWLEDGMENTS

We thank the Stracker and Boulton labs for support and input; T. Takaki for advice; G. Hewitt and R. O'Sullivan for critical reading of the manuscript; N. Pons, D. Fernandez, and N. Plana from the IRB Functional Genomics core for RNA-seq and ChIP-seq library preparation; A. Lladó, L. Bardia, and S. Tosi from the IRB Advanced Digital Microscopy facility for macro writing; O. Reina for assistance in Repbase analysis; M. Jiang and M. Howell from the Crick HTS platform for U-2-OS iCas9 cell line generation; the A. Jordan lab for reagents and advice to address repeat/IFN transcription; and the S. Peiro lab for advice on ATAC-seq. HeLa LT and GM847 cells were a kind gift from J. Jacobs/J. Karlseder and J. Lingner, respectively, and U-2-OS ΔPML cells were a kind gift from E. Lazzarini-Denchi. S.S.-B. was funded by a PhD fellowship and projects (100010434 and LCF/PR/GN14/10270002) from "la Caixa" Foundation and an EMBO long-term fellowship (ALTF 707-2019); M.V.-P. and M.S.-C. by FPI fellowships from the Ministry of Science, Innovation and Universities (MCIU); and L.M.K. by Else Kröner-Fresenius-Stiftung 2017_A50. Work in the S.J.B. lab is supported by the Francis Crick Institute, which receives core funding from Cancer Research UK (FC0010048), the UK Medical Research Council (FC0010048), and the Wellcome Trust (FC0010048). S.J.B. is also funded by an ERC advanced grant (TelMetab) and Wellcome Trust Senior Investigator and Collaborative Grants. T.H.S. was funded by the MCIU (BFU2015-68354/GENPATH, PGC2018-095616-B-I00/GINDATA, and FEDER), the Centres of Excellence Severo Ochoa award, and the CERCA Programme.

AUTHOR CONTRIBUTIONS

S.S.-B. and T.H.S. designed the study, interpreted the data, and cowrote the manuscript. S.S.-B. performed most of the experiments and analyzed data. M.V.-P., L.M.K., and M.S.-C. performed experiments. C.S.-O.A. analyzed sequencing and tumor data. T.H.S., S.J.B., and S.S.-B. secured funding and edited the manuscript. T.H.S. supervised the project.

DECLARATION OF INTERESTS

S.J.B. is also scientific co-founder and SVP of Science Strategy at Artios Pharma Ltd., Babraham, UK.

Received: March 25, 2020
Revised: June 30, 2020
Accepted: July 9, 2020
Published: August 4, 2020

REFERENCES

Alabert, C., Jasencakova, Z., and Groth, A. (2017). Chromatin replication and histone dynamics. *Adv. Exp. Med. Biol.* 1042, 311–333.

Ashburner, M., Ball, C.A., Blake, J.A., Botstein, D., Butler, H., Cherry, J.M., Davis, A.P., Dolinski, K., Dwight, S.S., Eppig, J.T., et al.; The Gene Ontology Consortium (2000). Gene ontology: tool for the unification of biology. *Nat. Genet.* 25, 25–29.

Bakhom, S.F., and Cantley, L.C. (2018). The multifaceted role of chromosomal instability in cancer and its microenvironment. *Cell* 174, 1347–1360.

Bakhom, S.F., Ngo, B., Laughney, A.M., Cavallo, J.-A., Murphy, C.J., Ly, P., Shah, P., Sriram, R.K., Watkins, T.B.K., Taunk, N.K., et al. (2018). Chromosomal instability drives metastasis through a cytosolic DNA response. *Nature* 553, 467–472.

Bao, W., Kojima, K.K., and Kohany, O. (2015). Repbase Update, a database of repetitive elements in eukaryotic genomes. *Mob. DNA* 6, 11.

Barroso-González, J., García-Expósito, L., Hoang, S.M., Lynskey, M.L., Roncaoli, J.L., Ghosh, A., Wallace, C.T., de Vitis, M., Modesti, M., Bernstein, K.A., et al. (2019). RAD51AP1 is an essential mediator of alternative lengthening of telomeres. *Mol. Cell* 76, 11–26.e7.

Bartkova, J., Horejsí, Z., Koed, K., Krämer, A., Tort, F., Zieger, K., Gulberg, P., Sehested, M., Nesland, J.M., Lukas, C., et al. (2005). DNA damage response as a candidate anti-cancer barrier in early human tumorigenesis. *Nature* 434, 864–870.

Benci, J.L., Xu, B., Qiu, Y., Wu, T.J., Dada, H., Twyman-Saint Victor, C., Cucolo, L., Lee, D.S.M., Pauken, K.E., Huang, A.C., et al. (2016). Tumor interferon signaling regulates a multigenic resistance program to immune checkpoint blockade. *Cell* 167, 1540–1554.e12.

Bester, A.C., Roniger, M., Oren, Y.S., Im, M.M., Sarni, D., Chaoat, M., Bension, A., Zamir, G., Shewach, D.S., and Kerem, B. (2011). Nucleotide deficiency promotes genomic instability in early stages of cancer development. *Cell* 145, 435–446.

Buenrostro, J.D., Giresi, P.G., Zaba, L.C., Chang, H.Y., and Greenleaf, W.J. (2013). Transposition of native chromatin for fast and sensitive epigenomic profiling of open chromatin, DNA-binding proteins and nucleosome position. *Nat. Methods* 10, 1213–1218.

Caballé Mestres, A., Berenguer Llergo, A., and Stephan-Otto Attolini, C. (2018). Adjusting for systematic technical biases in risk assessment of gene signatures in transcriptomic cancer cohorts. *bioRxiv*. <https://doi.org/10.1101/360495>.

Carrera, P., Moshkin, Y.M., Gronke, S., Sillje, H.H.W., Nigg, E.A., Jackle, H., and Karch, F. (2003). Touseled-like kinase functions with the chromatin assembly pathway regulating nuclear divisions. *Genes Dev.* 17, 2578–2590.

Carter, S.L., Eklund, A.C., Kohane, I.S., Harris, L.N., and Szallasi, Z. (2006). A signature of chromosomal instability inferred from gene expression profiles predicts clinical outcome in multiple human cancers. *Nat. Genet.* 38, 1043–1048.

Ceccarelli, M., Barthel, F.P., Malta, T.M., Sabedot, T.S., Salama, S.R., Murray, B.A., Morozova, O., Newton, Y., Radenbaugh, A., Pagnotta, S.M., et al.; TCGA Research Network (2016). Molecular profiling reveals biologically discrete subsets and pathways of progression in diffuse glioma. *Cell* 164, 550–563.

Cejka, P., Cannavo, E., Polaczek, P., Masuda-Sasa, T., Pokharel, S., Campbell, J.L., and Kowalczykowski, S.C. (2010). DNA end resection by Dna2-Sgs1-RPA and its stimulation by Top3-Rmi1 and Mre11-Rad50-Xrs2. *Nature* 467, 112–116.

Chen, Q., Sun, L., and Chen, Z.J. (2016). Regulation and function of the cGAS-STING pathway of cytosolic DNA sensing. *Nat. Immunol.* 17, 1142–1149.

Chen, Y.-A., Shen, Y.-L., Hsia, H.-Y., Tiang, Y.-P., Sung, T.-L., and Chen, L.-Y. (2017). Extrachromosomal telomere repeat DNA is linked to ALT development via cGAS-STING DNA sensing pathway. *Nat. Struct. Mol. Biol.* 24, 1124–1131.

Chiappinelli, K.B., Strissel, P.L., Desrichard, A., Li, H., Henke, C., Akman, B., Hein, A., Rote, N.S., Cope, L.M., Snyder, A., et al. (2015). Inhibiting DNA Methylation Causes an Interferon Response in Cancer via dsRNA Including Endogenous Retroviruses. *Cell* 162, 974–986.

Cho, N.W., Dilley, R.L., Lampson, M.A., and Greenberg, R.A. (2014). Interchromosomal homology searches drive directional ALT telomere movement and synapsis. *Cell* 159, 108–121.

Clément, C., Orsi, G.A., Gatto, A., Boyarchuk, E., Forest, A., Hajji, B., Miné-Hat-tab, J., Garnier, M., Gurard-Levin, Z.A., Quivy, J.-P., and Almouzni, G. (2018). High-resolution visualization of H3 variants during replication reveals their controlled recycling. *Nat. Commun.* 9, 3181.

- Cong, L., Ran, F.A., Cox, D., Lin, S., Barretto, R., Habib, N., Hsu, P.D., Wu, X., Jiang, W., Marraffini, L.A., and Zhang, F. (2013). Multiplex genome engineering using CRISPR/Cas systems. *Science* **339**, 819–823.
- Coquel, F., Silva, M.-J., Técher, H., Zadorozhny, K., Sharma, S., Niemniszczy, J., Mettling, C., Dardillac, E., Barthe, A., Schmitz, A.-L., et al. (2018). SAMHD1 acts at stalled replication forks to prevent interferon induction. *Nature* **557**, 57–61.
- Corpet, A., De Koning, L., Toedling, J., Savignoni, A., Berger, F., Lemaître, C., O'Sullivan, R.J., Karlseder, J., Barillot, E., Asselain, B., et al. (2011). Asf1b, the necessary Asf1 isoform for proliferation, is predictive of outcome in breast cancer. *EMBO J.* **30**, 480–493.
- Corpet, A., Olbrich, T., Gwerder, M., Fink, D., and Stucki, M. (2014). Dynamics of histone H3.3 deposition in proliferating and senescent cells reveals a DAXX-dependent targeting to PML-NBs important for pericentromeric heterochromatin organization. *Cell Cycle* **13**, 249–267.
- Curran, E., Chen, X., Corrales, L., Kline, D.E., Dubensky, T.W., Jr., Duttagupta, P., Kortylewski, M., and Kline, J. (2016). STING Pathway Activation Stimulates Potent Immunity against Acute Myeloid Leukemia. *Cell Rep.* **15**, 2357–2366.
- De Cecco, M., Ito, T., Petrashe, A.P., Elias, A.E., Skvir, N.J., Criscione, S.W., Caligiana, A., Broccoli, G., Adney, E.M., Boeke, J.D., et al. (2019). L1 drives IFN in senescent cells and promotes age-associated inflammation. *Nature* **566**, 73–78.
- Dilley, R.L., Verma, P., Cho, N.W., Winters, H.D., Wondisford, A.R., and Greenberg, R.A. (2016). Break-induced telomere synthesis underlies alternative telomere maintenance. *Nature* **539**, 54–58.
- Dillon, P.J., Gregory, S.M., Tamburro, K., Sanders, M.K., Johnson, G.L., Raab-Traub, N., Dittmer, D.P., and Damania, B. (2013). Twsled-like kinases modulate reactivation of gammaherpesviruses from latency. *Cell Host Microbe* **13**, 204–214.
- Drané, P., Ouararhni, K., Depaux, A., Shuaib, M., and Hamiche, A. (2010). The death-associated protein DAXX is a novel histone chaperone involved in the replication-independent deposition of H3.3. *Genes Dev.* **24**, 1253–1265.
- Draskovic, I., Arnoult, N., Steiner, V., Bacchetti, S., Lomonte, P., and Londoño-Vallejo, A. (2009). Probing PML body function in ALT cells reveals spatiotemporal requirements for telomere recombination. *Proc. Natl. Acad. Sci. USA* **106**, 15726–15731.
- Elsässer, S.J., Noh, K.-M., Diaz, N., Allis, C.D., and Banaszynski, L.A. (2015). Histone H3.3 is required for endogenous retroviral element silencing in embryonic stem cells. *Nature* **522**, 240–244.
- Ernst, J., and Kellis, M. (2012). ChromHMM: automating chromatin-state discovery and characterization. *Nat. Methods* **9**, 215–216.
- Feretzi, M., and Lingner, J. (2017). A practical qPCR approach to detect TERRA, the elusive telomeric repeat-containing RNA. *Methods* **114**, 39–45.
- Gagos, S., Chiourea, M., Christodoulidou, A., Apostolou, E., Raftopoulou, C., Deustch, S., Jefford, C.-E., Irminger-Finger, I., Shay, J.W., and Antonarakis, S.E. (2008). Pericentromeric instability and spontaneous emergence of human neoacrocentric and minute chromosomes in the alternative pathway of telomere lengthening. *Cancer Res.* **68**, 8146–8155.
- Gasser, S., Orsulic, S., Brown, E.J., and Raulet, D.H. (2005). The DNA damage pathway regulates innate immune system ligands of the NKG2D receptor. *Nature* **436**, 1186–1190.
- Goldberg, A.D., Banaszynski, L.A., Noh, K.-M., Lewis, P.W., Elsaesser, S.J., Stadler, S., Dewell, S., Law, M., Guo, X., Li, X., et al. (2010). Distinct factors control histone variant H3.3 localization at specific genomic regions. *Cell* **140**, 678–691.
- Gorgoulis, V.G., Vassiliou, L.-V.F., Karakaidos, P., Zacharatos, P., Kotsinas, A., Liloglou, T., Venere, M., Dittullo, R.A., Jr., Kastrinakis, N.G., Levy, B., et al. (2005). Activation of the DNA damage checkpoint and genomic instability in human precancerous lesions. *Nature* **434**, 907–913.
- Gravel, S., Chapman, J.R., Magill, C., and Jackson, S.P. (2008). DNA helicases Sgs1 and BLM promote DNA double-strand break resection. *Genes Dev.* **22**, 2767–2772.
- Grossman, R.L., Heath, A.P., Ferretti, V., Varmus, H.E., Lowy, D.R., Kibbe, W.A., and Staudt, L.M. (2016). Toward a shared vision for cancer genomic data. *N. Engl. J. Med.* **375**, 1109–1112.
- Groth, A., Lukas, J., Nigg, E.A., Silljé, H.H.W., Wernstedt, C., Bartek, J., and Hansen, K. (2003). Human Twsled like kinases are targeted by an ATM- and Chk1-dependent DNA damage checkpoint. *EMBO J.* **22**, 1676–1687.
- Groth, A., Corpet, A., Cook, A.J.L., Roche, D., Bartek, J., Lukas, J., and Almouzni, G. (2007). Regulation of replication fork progression through histone supply and demand. *Science* **318**, 1928–1931.
- Halazonetis, T.D., Gorgoulis, V.G., and Bartek, J. (2008). An oncogene-induced DNA damage model for cancer development. *Science* **319**, 1352–1355.
- Han, Z., Saam, J.R., Adams, H.P., Mango, S.E., and Schumacher, J.M. (2003). The *C. elegans* Twsled-like kinase (TLK-1) has an essential role in transcription. *Curr. Biol.* **13**, 1921–1929.
- Harding, S.M., Benci, J.L., Irianto, J., Discher, D.E., Minn, A.J., and Greenberg, R.A. (2017). Mitotic progression following DNA damage enables pattern recognition within micronuclei. *Nature* **548**, 466–470.
- Harrow, J., Frankish, A., Gonzalez, J.M., Tapanari, E., Diekhans, M., Kokocinski, F., Aken, B.L., Barrell, D., Zadissa, A., Searle, S., et al. (2012). GENCODE: the reference human genome annotation for The ENCODE Project. *Genome Res.* **22**, 1760–1774.
- Heijink, A.M., Talens, F., Jae, L.T., van Gijn, S.E., Fehrmann, R.S.N., Brummelkamp, T.R., and van Vugt, M.A.T.M. (2019). BRCA2 deficiency instigates cGAS-mediated inflammatory signaling and confers sensitivity to tumor necrosis factor- α -mediated cytotoxicity. *Nat. Commun.* **10**, 100.
- Heinz, S., Benner, C., Spann, N., Bertolino, E., Lin, Y.C., Laslo, P., Cheng, J.X., Murre, C., Singh, H., and Glass, C.K. (2010). Simple combinations of lineage-determining transcription factors prime cis-regulatory elements required for macrophage and B cell identities. *Mol. Cell* **38**, 576–589.
- Henson, J.D., Cao, Y., Huschtscha, L.I., Chang, A.C., Au, A.Y.M., Pickett, H.A., and Reddel, R.R. (2009). DNA C-circles are specific and quantifiable markers of alternative-lengthening-of-telomeres activity. *Nat. Biotechnol.* **27**, 1181–1185.
- Henson, J.D., Lau, L.M., Koch, S., Martin La Rotta, N., Dagg, R.A., and Reddel, R.R. (2017). The C-Circle Assay for alternative-lengthening-of-telomeres activity. *Methods* **114**, 74–84.
- Hoang, S.M., and O'Sullivan, R.J. (2020). Alternative lengthening of telomeres: building bridges to connect chromosome ends. *Trends Cancer* **6**, 247–260.
- Ishikawa, H., and Barber, G.N. (2008). STING is an endoplasmic reticulum adaptor that facilitates innate immune signalling. *Nature* **455**, 674–678.
- Izquierdo-Bouldstridge, A., Bustillos, A., Bonet-Costa, C., Aribau-Miralbés, P., García-Gomis, D., Dabad, M., Esteve-Codina, A., Pascual-Reguant, L., Peiró, S., Esteller, M., et al. (2017). Histone H1 depletion triggers an interferon response in cancer cells via activation of heterochromatic repeats. *Nucleic Acids Res.* **45**, 11622–11642.
- Kim, S. (2015). ppcor: An R package for a fast calculation to semi-partial correlation coefficients. *Commun. Stat. Appl. Methods* **22**, 665–674.
- Kim, J.-A., Tan, Y., Wang, X., Cao, X., Veeraraghavan, J., Liang, Y., Edwards, D.P., Huang, S., Pan, X., Li, K., et al. (2016). Comprehensive functional analysis of the twsled-like kinase 2 frequently amplified in aggressive luminal breast cancers. *Nat. Commun.* **7**, 12991.
- Kotsantis, P., Petermann, E., and Boulton, S.J. (2018). Mechanisms of Oncogene-Induced Replication Stress: Jigsaw Falling into Place. *Cancer Discov.* **8**, 537–555.
- Krause, D.R., Jonnalagadda, J.C., Gatei, M.H., Silljé, H.H.W., Zhou, B.-B., Nigg, E.A., and Khanna, K. (2003). Suppression of Twsled-like kinase activity after DNA damage or replication block requires ATM, NBS1 and Chk1. *Oncogene* **22**, 5927–5937.
- Kreienkamp, R., Graziano, S., Coll-Bonfill, N., Bedia-Diaz, G., Cybulla, E., Vindigni, A., Dorset, D., Kubben, N., Batista, L.F.Z., and Gonzalo, S. (2018). A Cell-Intrinsic Interferon-like Response Links Replication Stress to Cellular Aging Caused by Progerin. *Cell Rep.* **22**, 2006–2015.

- Lacoste, N., Woofe, A., Tachiwana, H., Garea, A.V., Barth, T., Cantaloube, S., Kurumizaka, H., Imhof, A., and Almouzni, G. (2014). Mislocalization of the centromeric histone variant CenH3/CENP-A in human cells depends on the chaperone DAXX. *Mol. Cell* **53**, 631–644.
- Langmead, B., Trapnell, C., Pop, M., and Salzberg, S.L. (2009). Ultrafast and memory-efficient alignment of short DNA sequences to the human genome. *Genome Biol.* **10**, R25.
- Lee, M., Teber, E.T., Holmes, O., Nones, K., Patch, A.-M., Dagg, R.A., Lau, L.M.S., Lee, J.H., Napier, C.E., Arthur, J.W., et al. (2018a). Telomere sequence content can be used to determine ALT activity in tumours. *Nucleic Acids Res.* **46**, 4903–4918.
- Lee, S.-B., Segura-Bayona, S., Villamor-Payà, M., Saredi, G., Todd, M.A.M., Attolini, C.S.-O., Chang, T.-Y., Stracker, T.H., and Groth, A. (2018b). Tousled-like kinases stabilize replication forks and show synthetic lethality with checkpoint and PARP inhibitors. *Sci. Adv.* **4**, eaat4985.
- Lelieveld, S.H., Reijnders, M.R.F., Pfundt, R., Yntema, H.G., Kamsteeg, E.-J., de Vries, P., de Vries, B.B.A., Willemsen, M.H., Kleefstra, T., Löhner, K., et al. (2016). Meta-analysis of 2,104 trios provides support for 10 new genes for intellectual disability. *Nat. Neurosci.* **19**, 1194–1196.
- Li, T., and Chen, Z.J. (2018). The cGAS-cGAMP-STING pathway connects DNA damage to inflammation, senescence, and cancer. *J. Exp. Med.* **215**, 1287–1299.
- Li, B., and Dewey, C.N. (2011). RSEM: accurate transcript quantification from RNA-Seq data with or without a reference genome. *BMC Bioinformatics* **12**, 323.
- Li, F., Deng, Z., Zhang, L., Wu, C., Jin, Y., Hwang, I., Vladimirova, O., Xu, L., Yang, L., Lu, B., et al. (2019). ATRX loss induces telomere dysfunction and necessitates induction of alternative lengthening of telomeres during human cell immortalization. *EMBO J.* **38**, e96659.
- Li, F., Huang, Q., Luster, T.A., Hu, H., Zhang, H., Ng, W.-L., Khodadadi-Jamayran, A., Wang, W., Chen, T., Deng, J., et al. (2020). In vivo epigenetic CRISPR screen identifies *Asf1a* as an immunotherapeutic target in Kras-mutant lung adenocarcinoma. *Cancer Discov.* **10**, 270–287.
- Liang, J., Zhao, H., Diplas, B.H., Liu, S., Liu, J., Wang, D., Lu, Y., Zhu, Q., Wu, J., Wang, W., et al. (2020). Genome-wide CRISPR-Cas9 screen reveals selective vulnerability of ATRX-mutant cancers to WEE1 inhibition. *Cancer Res.* **80**, 510–523.
- Liberzon, A., Subramanian, A., Pinchback, R., Thorvaldsdóttir, H., Tamayo, P., and Mesirov, J.P. (2011). Molecular signatures database (MSigDB) 3.0. *Bioinformatics* **27**, 1739–1740.
- Liberzon, A., Birger, C., Thorvaldsdóttir, H., Ghandi, M., Mesirov, J.P., and Tamayo, P. (2015). The Molecular Signatures Database (MSigDB) hallmark gene set collection. *Cell Syst.* **1**, 417–425.
- Loe, T.K., Li, J.S.Z., Zhang, Y., Azeroglu, B., Boddy, M.N., and Denchi, E.L. (2020). Telomere length heterogeneity in ALT cells is maintained by PML-dependent localization of the BTR complex to telomeres. *Genes Dev.* **34**, 650–662.
- Love, M.I., Huber, W., and Anders, S. (2014). Moderated estimation of fold change and dispersion for RNA-seq data with DESeq2. *Genome Biol.* **15**, 550.
- Lovejoy, C.A., Li, W., Reisenweber, S., Thongthip, S., Bruno, J., de Lange, T., De, S., Petri, J.H.J., Sung, P.A., Jasin, M., et al.; ALT Starr Cancer Consortium (2012). Loss of ATRX, genome instability, and an altered DNA damage response are hallmarks of the alternative lengthening of telomeres pathway. *PLoS Genet.* **8**, e1002772.
- Macheret, M., and Halazonetis, T.D. (2018). Intragenic origins due to short G1 phases underlie oncogene-induced DNA replication stress. *Nature* **555**, 112–116.
- Mackenzie, K.J., Carroll, P., Martin, C.-A., Murina, O., Fluteau, A., Simpson, D.J., Olova, N., Sutcliffe, H., Rainger, J.K., Leitch, A., et al. (2017). cGAS surveillance of micronuclei links genome instability to innate immunity. *Nature* **548**, 461–465.
- Marzec, P., Armenise, C., Pérot, G., Roumelioti, F.-M., Basyuk, E., Gagos, S., Chibon, F., and Déjardin, J. (2015). Nuclear-receptor-mediated telomere insertion leads to genome instability in ALT cancers. *Cell* **160**, 913–927.
- Murga, M., Campaner, S., Lopez-Contreras, A.J., Toledo, L.I., Soria, R., Montaña, M.F., Artista, L., Schleker, T., Guerra, C., Garcia, E., et al. (2011). Exploiting oncogene-induced replicative stress for the selective killing of Myc-driven tumors. *Nat. Struct. Mol. Biol.* **18**, 1331–1335.
- Nimonkar, A.V., Genschel, J., Kinoshita, E., Polaczek, P., Campbell, J.L., Wyman, C., Modrich, P., and Kowalczykowski, S.C. (2011). BLM-DNA2-RPA-MRN and EXO1-BLM-RPA-MRN constitute two DNA end resection machineries for human DNA break repair. *Genes Dev.* **25**, 350–362.
- Novellino, F., Saccà, V., Donato, A., Zaffino, P., Spadea, M.F., Vismara, M., Arcidiacono, B., Malara, N., Presta, I., and Donato, G. (2020). Innate Immunity: A Common Denominator between Neurodegenerative and Neuropsychiatric Diseases. *Int. J. Mol. Sci.* **21**, 1115.
- O’Sullivan, R.J., Arnoult, N., Lackner, D.H., Oganessian, L., Haggblom, C., Corpet, A., Almouzni, G., and Karlseder, J. (2014). Rapid induction of alternative lengthening of telomeres by depletion of the histone chaperone ASF1. *Nat. Struct. Mol. Biol.* **21**, 167–174.
- Panier, S., Maric, M., Hewitt, G., Mason-Osann, E., Gali, H., Dai, A., Labadorf, A., Guervilly, J.-H., Ruis, P., Segura-Bayona, S., et al. (2019). SLX4IP Antagonizes Promiscuous BLM Activity during ALT Maintenance. *Mol. Cell* **76**, 27–43.e11.
- Pasero, P., and Vindigni, A. (2017). Nucleases Acting at Stalled Forks: How to Reboot the Replication Program with a Few Shortcuts. *Annu. Rev. Genet.* **51**, 477–499.
- Pilyugin, M., Demmers, J., Verrijzer, C.P., Karch, F., and Moshkin, Y.M. (2009). Phosphorylation-mediated control of histone chaperone ASF1 levels by Tousled-like kinases. *PLoS ONE* **4**, e8328.
- R Core Team (2016).** R: A Language and Environment for Statistical Computing (Vienna, Austria: R Foundation for Statistical Computing). <https://www.R-project.org/>.
- Ramanjulu, J.M., Pesiridis, G.S., Yang, J., Concha, N., Singhaus, R., Zhang, S.-Y., Tran, J.-L., Moore, P., Lehmann, S., Eberl, H.C., et al. (2018). Design of amidobenzimidazole STING receptor agonists with systemic activity. *Nature* **564**, 439–443.
- Reijnders, M.R.F., Miller, K.A., Alvi, M., Goos, J.A.C., Lees, M.M., de Burca, A., Henderson, A., Kraus, A., Mikat, B., de Vries, B.B.A., et al.; Deciphering Developmental Disorders Study (2018). De Novo and Inherited Loss-of-Function Variants in TLK2: Clinical and Genotype-Phenotype Evaluation of a Distinct Neurodevelopmental Disorder. *Am. J. Hum. Genet.* **102**, 1195–1203.
- Reisländer, T., Lombardi, E.P., Groelly, F.J., Miar, A., Porru, M., Di Vito, S., Wright, B., Lockstone, H., Biroccio, A., Harris, A., et al. (2019). BRCA2 abrogation triggers innate immune responses potentiated by treatment with PARP inhibitors. *Nat. Commun.* **10**, 3143.
- Rodier, F., Coppé, J.-P., Patil, C.K., Hoeijmakers, W.A.M., Muñoz, D.P., Raza, S.R., Freund, A., Campeau, E., Davalos, A.R., and Campisi, J. (2009). Persistent DNA damage signalling triggers senescence-associated inflammatory cytokine secretion. *Nat. Cell Biol.* **11**, 973–979.
- Roe, J.L., Rivin, C.J., Sessions, R.A., Feldmann, K.A., and Zambryski, P.C. (1993). The Tousled gene in *A. thaliana* encodes a protein kinase homolog that is required for leaf and flower development. *Cell* **75**, 939–950.
- Segura-Bayona, S., and Stracker, T.H. (2019). The Tousled-like kinases regulate genome and epigenome stability: implications in development and disease. *Cell. Mol. Life Sci.* **76**, 3827–3841.
- Silljé, H.H., and Nigg, E.A. (2001). Identification of human *Asf1* chromatin assembly factors as substrates of Tousled-like kinases. *Curr. Biol.* **11**, 1068–1073.
- Silljé, H.H., Takahashi, K., Tanaka, K., Van Houwe, G., and Nigg, E.A. (1999). Mammalian homologues of the plant Tousled gene code for cell-cycle-regulated kinases with maximal activities linked to ongoing DNA replication. *EMBO J.* **18**, 5691–5702.

- Sobinoff, A.P., Allen, J.A., Neumann, A.A., Yang, S.F., Walsh, M.E., Henson, J.D., Reddel, R.R., and Pickett, H.A. (2017). BLM and SLX4 play opposing roles in recombination-dependent replication at human telomeres. *EMBO J.* **36**, 2907–2919.
- Steed, A., Buch, T., Waisman, A., and Virgin, H.W., 4th. (2007). Gamma interferon blocks gammaherpesvirus reactivation from latency in a cell type-specific manner. *J. Virol.* **81**, 6134–6140.
- Subramanian, A., Tamayo, P., Mootha, V.K., Mukherjee, S., Ebert, B.L., Gillette, M.A., Paulovich, A., Pomeroy, S.L., Golub, T.R., Lander, E.S., and Mesirov, J.P. (2005). Gene set enrichment analysis: a knowledge-based approach for interpreting genome-wide expression profiles. *Proc. Natl. Acad. Sci. USA* **102**, 15545–15550.
- Taylor, A.M., Shih, J., Ha, G., Gao, G.F., Zhang, X., Berger, A.C., Schumacher, S.E., Wang, C., Hu, H., Liu, J., et al.; Cancer Genome Atlas Research Network (2018). Genomic and functional approaches to understanding cancer aneuploidy. *Cancer Cell* **33**, 676–689.e3.
- Thorsson, V., Gibbs, D.L., Brown, S.D., Wolf, D., Bortone, D.S., Ou Yang, T.-H., Porta-Pardo, E., Gao, G.F., Plaisier, C.L., Eddy, J.A., et al.; Cancer Genome Atlas Research Network (2018). The immune landscape of cancer. *Immunity* **48**, 812–830.e14.
- Toledo, L.I., Murga, M., and Fernandez-Capetillo, O. (2011). Targeting ATR and Chk1 kinases for cancer treatment: a new model for new (and old) drugs. *Mol. Oncol.* **5**, 368–373.
- Tripathi, V., Agarwal, H., Priya, S., Batra, H., Modi, P., Pandey, M., Saha, D., Raghavan, S.C., and Sengupta, S. (2018). MRN complex-dependent recruitment of ubiquitylated BLM helicase to DSBs negatively regulates DNA repair pathways. *Nat. Commun.* **9**, 1016.
- Udugama, M., M Chang, F.T., Chan, F.L., Tang, M.C., Pickett, H.A.R., R McGhie, J.D., Mayne, L., Collas, P., Mann, J.R., and Wong, L.H. (2015). Histone variant H3.3 provides the heterochromatic H3 lysine 9 tri-methylation mark at telomeres. *Nucleic Acids Res.* **43**, 10227–10237.
- Wu, L., Cao, J., Cai, W.L., Lang, S.M., Horton, J.R., Jansen, D.J., Liu, Z.Z., Chen, J.F., Zhang, M., Mott, B.T., et al. (2018). KDM5 histone demethylases repress immune response via suppression of STING. *PLoS Biol.* **16**, e2006134.
- Xia, T., Konno, H., Ahn, J., and Barber, G.N. (2016). Deregulation of STING signaling in colorectal carcinoma constrains DNA damage responses and correlates with tumorigenesis. *Cell Rep.* **14**, 282–297.
- Yadav, T., Quivy, J.-P., and Almouzni, G. (2018). Chromatin plasticity: A versatile landscape that underlies cell fate and identity. *Science* **361**, 1332–1336.
- Zevini, A., Olganier, D., and Hiscott, J. (2017). Crosstalk between Cytoplasmic RIG-I and STING Sensing Pathways. *Trends Immunol.* **38**, 194–205.
- Zhang, Y., Liu, T., Meyer, C.A., Eeckhoute, J., Johnson, D.S., Bernstein, B.E., Nusbaum, C., Myers, R.M., Brown, M., Li, W., and Liu, X.S. (2008). Model-based analysis of ChIP-Seq (MACS). *Genome Biol.* **9**, R137.
- Zhang, H., Pandey, S., Travers, M., Sun, H., Morton, G., Madzo, J., Chung, W., Khowsathit, J., Perez-Leal, O., Barrero, C.A., et al. (2018). Targeting CDK9 reactivates epigenetically silenced genes in cancer. *Cell* **175**, 1244–1258.e26.
- Zhong, B., Yang, Y., Li, S., Wang, Y.-Y., Li, Y., Diao, F., Lei, C., He, X., Zhang, L., Tien, P., and Shu, H.B. (2008). The adaptor protein MITA links virus-sensing receptors to IRF3 transcription factor activation. *Immunity* **29**, 538–550.
- Zhu, L.J., Gazin, C., Lawson, N.D., Pagès, H., Lin, S.M., Lapointe, D.S., and Green, M.R. (2010). ChIPpeakAnno: a Bioconductor package to annotate ChIP-seq and ChIP-chip data. *BMC Bioinformatics* **11**, 237.

STAR★METHODS

KEY RESOURCES TABLE

REAGENT or RESOURCE	SOURCE	IDENTIFIER
Antibodies		
Rabbit polyclonal anti-TLK1	Cell Signaling Technology	Cat# 4125; RRID:AB_2203885
Rabbit polyclonal anti-TLK2	Bethyl Laboratories	Cat# A301-257A; RRID:AB_890676
Rabbit polyclonal anti-phospho RPA32 (S4/S8)	Bethyl Laboratories	Cat# A300-245A; RRID:AB_210547
Rabbit polyclonal anti-phospho RPA32 (S33)	Bethyl Laboratories	Cat# A300-246A; RRID:AB_2180847
Mouse monoclonal anti-RPA32, clone RPA34-20	Calbiochem	Cat# NA19L; RRID:AB_565123
Rabbit polyclonal anti-phospho H2AX (S139) (γ H2AX)	Santa Cruz Biotechnology	Cat# sc-101696; RRID:AB_2114997
Rabbit polyclonal anti-phospho H2AX (S139) (γ H2AX)	Cell Signaling Technology	Cat# 2577; RRID:AB_2118010
Rabbit polyclonal anti-phospho p53 (S15)	Cell Signaling Technology	Cat# 9284; RRID:AB_331464
Mouse monoclonal anti-MRE11, clone 18	Santa Cruz Biotechnology	Cat# sc-135992; RRID:AB_2145244
Rabbit polyclonal anti-BLM	Abcam	Cat# ab2179; RRID:AB_2290411
Mouse monoclonal anti-STING/TMEM173, clone 723505	R&D Systems	Cat# MAB7169; RRID:AB_10971940
Rabbit monoclonal anti-cGAS, clone D1D3G	Cell Signaling Technology	Cat# 15102; RRID:AB_2732795
Rabbit monoclonal anti-RIG-I, clone D14G6	Cell Signaling Technology	Cat# 3743; RRID:AB_2269233
Rabbit monoclonal anti-MDA5, clone D74E4	Cell Signaling Technology	Cat# 5321; RRID:AB_10694490
Mouse monoclonal anti-HP1 α , clone 2HP1H5	Active Motif	Cat# 39977; RRID:AB_2614983
Mouse monoclonal anti-PML, clone PG-M3	Santa Cruz Biotechnology	Cat# sc-966; RRID:AB_628162
Rabbit polyclonal anti-TRF2	Novus Biologicals	Cat# NB110-57130; RRID:AB_844199
Mouse monoclonal anti-TRF1, clone TRF-78	Abcam	Cat# ab10579; RRID:AB_2201461
Rabbit polyclonal anti-H3.3	EMD Millipore	Cat# 09-838; RRID:AB_10845793
Rabbit polyclonal anti-Histone H3 (tri methyl K9) (H3K9me3)	Abcam	Cat# ab8898; RRID:AB_306848
Goat anti-Mouse IgG (H+L) Secondary Antibody, HRP	Thermo Fisher Scientific	Cat# 31430; RRID:AB_228307
Polyclonal Goat Anti-Mouse Immunoglobulins/HRP	Agilent-Dako	Cat# P0447; RRID:AB_2617137
Polyclonal Swine Anti-Rabbit Immunoglobulins/HRP	Agilent-Dako	Cat# P0399; RRID:AB_2617141
Alexa Fluor 488 Goat anti-Rabbit IgG (H+L)	Thermo Fisher Scientific	Cat# A11008; RRID:AB_143165
Alexa Fluor 488 Goat anti-Mouse IgG (H+L)	Thermo Fisher Scientific	Cat# A11001; RRID:AB_2534069
Alexa Fluor 568 Goat anti-Rabbit IgG (H+L)	Thermo Fisher Scientific	Cat# A11011; RRID:AB_143157
Alexa Fluor 568 Goat anti-Mouse IgG (H+L)	Thermo Fisher Scientific	Cat# A11004; RRID:AB_2534072
Bacterial and Virus Strains		
Bacteria: TOP10 Chemically Competent <i>E. coli</i>	Thermo Fisher Scientific	Cat# C404006
Lentivirus: pLKO.1-puro-shScramble control	IRB Functional Genomics Core	Cat# SHC002
Lentivirus: pLKO.1-puro-shSTING	IRB Functional Genomics Core	Cat# TRCN0000163296
Chemicals, Peptides, and Recombinant Proteins		
Hydroxyurea	Sigma-Aldrich	Cat# H8627
Aphidicolin	Calbiochem	Cat# 178273, CAS 38966-21-1
Roscovitine	Tocris	Cat# 1332
Mirin	Tocris	Cat# 3190
BX-795	Selleckchem	Cat# S1274
Lipofectamine 2000 Transfection Reagent	Thermo Fisher Scientific	Cat# 11668027
Lipofectamine RNAiMAX Transfection Reagent	Thermo Fisher Scientific	Cat# 13778150
Dynabeads Protein G	Thermo Fisher Scientific	Cat# 10004D
4',6-Diamidino-2-phenylindole dihydrochloride (DAPI)	Sigma-Aldrich	Cat# 32670
VECTASHIELD Antifade Mounting Medium	Vector Laboratories	Cat# H-1000

(Continued on next page)

Continued

REAGENT or RESOURCE	SOURCE	IDENTIFIER
ProLong Gold Antifade Mountant with DAPI	Thermo Fisher Scientific	Cat# P36935
Crystal Violet	Sigma-Aldrich	Cat# HT90132
phi29 DNA Polymerase	NEB	Cat# M0269L
phi29 DNA Polymerase	Thermo Fisher Scientific	Cat# EP0092
ATP, [γ - ³² P]- 6000Ci/mmol 10mCi/ml	Perkin Elmer	Cat# NEG502Z250UC
Phosphatase Inhibitor Cocktail 2	Sigma-Aldrich	Cat# P5726
Phosphatase Inhibitor Cocktail 3	Sigma-Aldrich	Cat# P0044
cComplete, EDTA-free Protease Inhibitor Cocktail	Roche	Cat# 04693132001
M-PER Mammalian Protein Extraction Reagent	Thermo Fisher Scientific	Cat# 78503
T4 Polynucleotide Kinase	NEB	Cat# M0236S
MinElute PCR Purification Kit	QIAGEN	Cat# 28004
PureLink Quick Gel Extraction & PCR Purification Combo Kit	Thermo Fisher Scientific	Cat# K220001
Pierce Recombinant Protein A/G, Peroxidase Conjugated	Thermo Fisher Scientific	Cat# 32490
Critical Commercial Assays		
Nextera DNA Library Preparation Kit	Illumina	Cat# FC-121-1030
NEBNext High-Fidelity 2X PCR Master Mix	NEB	Cat# M0541S
High-Capacity cDNA Reverse Transcription Kit	Thermo Fisher Scientific	Cat# 4368814
PureLink RNA Mini Kit	Thermo Fisher Scientific	Cat# 12183018A
Ribo-Zero Gold rRNA Removal Kit (Human/Mouse/Rat)	Illumina	Cat# RZHM11106
NEBNext Ultra II DNA Library Prep Kit for Illumina	NEB	Cat# E7645S
BD OptEIA Human IP-10 ELISA Kit	BD Bioscience	Cat# 550926
2'3'-cGAMP ELISA Kit	Cayman Chemical	Cat# 501700
Qubit dsDNA HS Assay Kit	Thermo Fisher Scientific	Cat# Q32854
Telomere PNA FISH Kit/Cy3	Agilent-Dako	Cat# K5326
TelC-FITC	PNA Bio	Cat# F1009
Deposited Data		
Raw and processed data (ATAC-Seq in U-2-OS)	This study	GSE131023 Table S1
Raw and processed data (ATAC-Seq in HeLa LT)	This study	GSE131023 Table S2
Raw and processed data (H3.3 ChIP-Seq in U-2-OS)	This study	GSE131023 Table S3
Raw and processed data (RNA-Seq in U-2-OS)	This study	GSE131023 Tables S4 and S5
Experimental Models: Cell Lines		
Human: U-2-OS	ATCC	RRID:CVCL_0042
Human: HeLa LT	Gift from J. Jacobs / J. Karlseder	O'Sullivan et al., 2014
Human: GM847	Gift from J. Lingner	RRID:CVCL_7908
Human: RPE-1 hTERT	The Francis Crick Institute Cell Services	RRID:CVCL_4388
Human: AD293	Stratagene	RRID:CVCL_9804
Human: HEK293	The Francis Crick Institute Cell Services	RRID:CVCL_0045
Human: U-2-OS Δ TLK1	This study	N/A
Human: U-2-OS Δ PML clone #15G4	Gift from E. Lazzerini-Denchi	Loe et al., 2020
Human: HeLa LT Δ TLK1 clone #5	This study	N/A

(Continued on next page)

Continued

REAGENT or RESOURCE	SOURCE	IDENTIFIER
Human: HeLa LT ΔTLK1 clone #8	This study	N/A
Human: HeLa LT ΔTLK1 clone #12	This study	N/A
Human: U-2-OS iCas9 clone #5	This study	N/A
Experimental Models: Organisms/Strains		
N/A		
Oligonucleotides		
ON-TARGETplus Non-targeting Control Pool	Dharmacon	D-001810-10
ON-TARGET plus SMARTpool human TLK1	Dharmacon	L-004174-00
ON-TARGET plus SMARTpool human TLK2	Dharmacon	L-005389-00
ON-TARGET plus SMARTpool human BLM	Dharmacon	L-007287-00
Human SAMHD1_7 FlexiTube siRNA	QIAGEN	Cat# SI04243673
siMRE11 (5'-GCUAAUGACUCUGAUGAUA-3')	Thermo Fisher Scientific	Tripathi et al., 2018
siTLK1 (5'-GAAGCUCGGUCUAUUGUAA-3')	Thermo Fisher Scientific	Lee et al., 2018b
siTLK2#1 (5'-GGAGGGGAGAAUAGAUGAU-3')	Thermo Fisher Scientific	Lee et al., 2018b
siTLK2#2 (5'-GGAAAGGAUAAAUCACAG-3')	Thermo Fisher Scientific	Lee et al., 2018b
siTLK2#9 (5'-GAUAGAAAGACAACGGAAA-3')	Dharmacon	J-005389-09
siASF1a (5'-AAGUGAAGAAUACGAUCAAGU-3')	Thermo Fisher Scientific	Lee et al., 2018b
siASF1b (5'-AACACGAGUACCUCAACCCU-3')	Thermo Fisher Scientific	Lee et al., 2018b
siH3.3#A (5'-CUACAAAAGCCGCUCGCAA-3')	Thermo Fisher Scientific	Corpet et al., 2014
siH3.3#B (5'-GCUAAGAGAGUCACCAUCA-3')	Thermo Fisher Scientific	Corpet et al., 2014
siGL2 (5'-CGUACGCGAAUACUUCGA-3')	Thermo Fisher Scientific	Lee et al., 2018b
siGFP (5'-GGCUACGUCCAGGAGCGCCGACC-3')	Thermo Fisher Scientific	Lee et al., 2018b
Guide RNA sequence targeting human TLK1 exon 10 (5'-TAACTGTTGTAAGTGCCCG-3')	Sigma-Aldrich	N/A
Edit-R tracrRNA	Dharmacon	U-002005
Edit-R Synthetic crRNA Non-targeting Control	Dharmacon	U-007503-01
Edit-R Human MB21D1/cGAS crRNA	Dharmacon	CM-015607-03
Edit-R Human DDX58/RIG-I crRNA	Dharmacon	CM-012511-01
Edit-R Human IFIH1/MDA5 crRNA	Dharmacon	CM-013041-01
See Table S6 for additional oligonucleotides used for ATAC library preparation, RT-qPCR assays, C-circle assay probes	Sigma-Aldrich	N/A
Recombinant DNA		
pX330-CRISPR-Cas9-SV40prom-EGFP	Gift from C. Cortina, E. Battle laboratory	Cong et al., 2013
pHFUW-Flag-TRF1-FokI WT	Gift from R. Greenberg	Cho et al., 2014
pHFUW-Flag-TRF1-FokI D450A	Gift from R. Greenberg	Cho et al., 2014
Software and Algorithms		
Fiji	NIH	https://fiji.sc/
Cell Profiler	Broad Institute	https://cellprofiler.org
Prism 8	GraphPad Software	https://www.graphpad.com/
Adobe Photoshop 2020	Adobe	https://www.adobe.com/uk/products/photoshop.html
Adobe Illustrator 2020	Adobe	https://www.adobe.com/uk/products/illustrator.html
R	R core team	https://www.r-project.org/
Bowtie v0.12.9	Langmead et al., 2009	http://bowtie-bio.sourceforge.net/
Sambamba v0.5.8	N/A	http://lomereiter.github.io/sambamba/
MACS v1.4.2	Zhang et al., 2008	http://liulab.dfci.harvard.edu/MACS/

(Continued on next page)

Continued

REAGENT or RESOURCE	SOURCE	IDENTIFIER
HOMER v2.8.2	Heinz et al., 2010	http://homer.ucsd.edu/
Rsamtools R package (version 1.30.0)	N/A	http://bioconductor.org/packages/release/bioc/html/Rsamtools.html
DESeq2	Love et al., 2014	https://bioconductor.org/packages/release/bioc/html/DESeq2.html
ChIPpeakAnno R package	Zhu et al., 2010	https://bioconductor.org/packages/release/bioc/html/ChIPpeakAnno.html
Geneset Enrichment Analysis (GSEA)	Subramanian et al., 2005	https://www.gsea-msigdb.org/gsea/
Gene Ontology (GO) terms	Ashburner et al., 2000	http://geneontology.org/
GSEABase R package (version 1.40.1)	TU Dortmund	http://bioconductor.org/packages/release/bioc/html/GSEABASE.html
The Molecular Signatures Database (MSigDB)	Liberzon et al., 2011	https://www.gsea-msigdb.org/gsea/
Hallmark collection from MSigDB	Liberzon et al., 2015	https://www.gsea-msigdb.org/gsea/
Gencode annotation (version 19)	Harrow et al., 2012	https://www.genecodegenes.org/
Repbse database (version 22.06)	Bao et al., 2015	https://www.girinst.org/repbse/
Other		
Nunc 8-well Lab-Tek II Chamber Slide	Thermo Fisher Scientific	Cat# 154534PK
Leica TCS SPE confocal system	Leica	DM2500
Olympus IX83 inverted microscope, ScanR	Olympus	N/A
Bioruptor Pico sonication device	Diagenode	Cat# B01060010
2100 Bioanalyzer Instrument	Agilent	Cat# G2939BA

RESOURCE AVAILABILITY

Lead Contact

Further information and requests for resources, reagents, data or code should be directed to and will be fulfilled by the Lead Contact, Travis H. Stracker (travis.stracker@nih.gov).

Materials Availability

Materials generated in this study are available upon request from the Lead Contact.

Data and Code Availability

The accession number for the datasets reported in this paper (ATAC-seq (U-2-OS and HeLa LT), H3.3 ChIP-seq (U-2-OS) and RNA-seq (U-2-OS)) are GEO: GSE131023. <https://www.ncbi.nlm.nih.gov/geo/> The computer code generated during the current study is available on reasonable request.

EXPERIMENTAL MODEL AND SUBJECT DETAILS

Cell lines

Human cell lines used in this study are reported in the [Key Resources Table](#). Cells were grown in DMEM (Thermo Fisher Scientific) supplemented with 10% FBS (Sigma-Aldrich) and penicillin–streptomycin at 37°C in a 5% CO₂ incubator. Knockout ΔTLK1 U-2-OS and HeLa LT cell lines were generated using CRISPR/Cas9 genome editing. Guide RNA sequence targeting human TLK1 exon 10 was cloned into the plasmid pX330-CRISPR-Cas9-SV40prom-EGFP (Cong et al., 2013) after digestion with BbsI (NEB). Cells were transfected using Lipofectamine 2000 (Thermo Fisher Scientific) with the corresponding pX330-CRISPR-Cas9-SV40prom-EGFP plasmid and 48 hours following transfection, single cells positive for GFP were FACS-sorted (BD FACSAria III) at a ratio of 1 cell per well in 96 well plates. Single cell clones were expanded and screened by Western Blot for protein levels of TLK1. For lentiviral transductions of shRNA against STING, AD293 producer cells were transfected using PEI (Polysciences Inc.) with 10 μg of pLKO.1-puro-shScramble control (SHC002) or pLKO.1-puro-shSTING (TRCN0000163296) and with lentiviral packaging vectors (2 μg REV, 6 μg RRE and 2 μg VSV-G). Medium was refreshed 8 h after transfection and viral supernatants were collected and filtered through a 0.45 μm filter at approximately 48 and 72 h post-transfection. For infection, cells were overlaid with filtered viral supernatant supplemented with 8 μg/ml Polybrene (Sigma-Aldrich) twice to achieve optimal infection efficiency. Cells were selected with 1 μg/ml

of puromycin. U-2-OS cells expressing inducible Cas9 (iCas9) were generated by lentiviral transduction of Edit-R Inducible Cas9 (Dharmacon). Single cell clones were expanded and screened for Cas9 activity.

METHOD DETAILS

Drug treatments

For drug treatment we used: Hydroxyurea (Sigma), Aphidicolin (Calbiochem) at the indicated doses; Roscovitine (Tocris), 50 μ M for 5 hours; Mirin (Tocris), 50 μ M for 5 hours; BX795 (Selleckchem), 1 μ M for 24 hours. For serum starvation experiments, after cell attachment the medium was replaced with low-serum media (0.25% FBS) for serum-starved cells and with fresh media (10% FBS) for asynchronous cells. After 24 h, medium was replaced again (0.25% FBS for serum starved cells; 10% FBS for control cells) until cells were harvested.

siRNA/crRNA transfections

For siRNA transfection, cells were transfected with siRNAs (Sigma-Aldrich or Dharmacon) at a final concentration of 100 nM using Lipofectamine RNAiMAX (Thermo Fisher Scientific). Transfections were done on attached cells that had been plated for approximately 18 hours, in media without antibiotics and the transfection mix was prepared in Opti-MEM (Thermo Fisher Scientific). Cells were transfected once and either split for several experiments after 24 hours and harvested after additional 24-72 hours or directly harvested 48-96 hours post-transfection. We used luciferase and GFP targeting or non-targeting siRNA as mock negative controls (siCont). The siRNAs used in this study are listed in the [Key Resources Table](#).

For crRNA transfection, cells were transfected with crRNA and tracrRNA (1:1 ratio) (Dharmacon) at a final concentration of 50 nM using Lipofectamine RNAiMAX (Thermo Fisher Scientific). Transfection was done in attached cells in media without antibiotics and induction of Cas9 by 1 μ g/ml Doxycycline. The transfection mix was prepared in Opti-MEM (Thermo Fisher Scientific). Knockout was assessed 72-120 h after transfection. The crRNAs used in this study are listed in the [Key Resources Table](#).

Western blot analysis

Cells were collected after two cold PBS washes by scraping in 2X SDS Lysis Buffer (4% SDS, 20% Glycerol, 120 mM Tris-Cl pH 6.8, 1x protease (Roche) and phosphatase inhibitors (Sigma-Aldrich)) on ice. Lysates were sonicated at medium-high intensity for 10 minutes in a Bioruptor Standard (Diagenode) placed at 4°C and subsequently boiled for 10 minutes at 90°C. Proteins were quantified using the DC Protein Assay (Bio-Rad), separated by SDS-PAGE and transferred to 0.2 μ m pore Nitrocellulose membrane (Amersham Protran; Sigma-Aldrich). Membranes blocked with 5% milk/PBST for 1 h at room temperature and probed with primary antibodies overnight at 4°C. These were detected with appropriate secondary antibodies conjugated to HRP and visualized by ECL-Plus (GE Healthcare).

Cytokine Detection

For CXCL10 detection, medium was replaced 48 hours after siRNA transfection and CXCL10 was measured after additional 24 hours in the supernatant of the cells using BD OptEIA Human IP-10 ELISA Kit (BD Bioscience) according to the manufacturer's protocol. For CXCL10 detection on U-2-OS iCas9 cells, medium was replaced 48 hours after crRNA transfection and 24 hours after siRNA transfection and CXCL10 was measured after additional 72 hours. ELISA assays were carried out in technical duplicate or triplicate.

2'3'-cGAMP ELISA

HeLa LT and U-2-OS were seeded in 12-well plates, transfected with siRNA and 24 h later cells were split and seeded in 6-well plates. For stimulation with dsDNA90, cells were seeded in 6-well plates and transfected with 4 μ g/ml using Lipofectamine 2000 (Thermo Fisher Scientific). 72 h after siRNA treatment and 24 h after dsDNA90 transfection, cells were harvested, counted, washed with PBS, pelleted, and stored at -80° C. To quantify 2'3'-cGAMP levels, pellets corresponding to 250,000 cells (U-2-OS) or 500,000 cells (HeLa LT) were resuspended in 130 μ L M-PER buffer (Thermo Fisher Scientific), incubated on ice for 15 min, centrifuged at 16,000 g at 4°C and 2'3'-cGAMP levels were quantified using the 2'3'-cGAMP ELISA Kit (Cayman Chemical) in technical duplicate according to the manufacturer's instructions.

Immunofluorescence (IF) and IF-FISH

For IF of chromatin-bound proteins, cells were grown on 8-well Lab Tek II chamber slides (Labclinics) to sub-confluence. For regular IF, cells were grown on Poly-L-Lysine coated coverslips. For chromatin-bound proteins, pre-extraction was performed using cold 0.2% Triton X-100 in 1X PBS on ice for 5 minutes. Cells were fixed for 10 minutes in 4% paraformaldehyde at room temperature and permeabilized for 5 minutes in 0.2% Triton in 1X PBS at room temperature. After two washes in PBS, fixed cells were incubated for 1 h in blocking solution (3% BSA 0.1% Tween/PBS) and stained using primary antibodies diluted 1:250 in blocking solution for 4 h at room temperature in a humid chamber. The secondary antibodies were used at a dilution of 1:500 in blocking solution. Slides were mounted in Vectashield (Vector Laboratories).

For IF-FISH, after standard IF staining with primary and secondary antibody incubations, washes were performed with IF blocking solution. To continue with FISH, slides were fixed again in 4% formaldehyde for 5 min at room temperature, washed in PBS and

dehydrated in increasing concentrations of ethanol (70%, 95%, and 100%). The slides were air-dried, incubated with Telomere PNA Probe/Cy3 (Dako-Agilent) or TelC-FITC (PNA Bio) and denatured on an 80°C hot plate for 5-10 minutes. Hybridization took place in the dark for 3-4 hours at room temperature. The slides were subsequently washed in Rinse and pre-heated Wash Solutions (Dako-Agilent) or in wash solution (70% Formamide, 10 mM Tris-HCl pH 7.2) and dehydrated in increasing concentrations of ethanol (70%, 95%, and 100%). Slides were washed in DAPI and mounted in Vectashield (Vector Laboratories).

Confocal fluorescence images were obtained on a Leica DM2500 SPE confocal system. Images were taken with 40x NA 1.15 oil or 63x NA 1.3 oil objectives and the standard LAS-AF software. For high-throughput microscopy (HTM), 24-48 images were automatically acquired from each well with a robotized fluorescence microscopy station (Scan'R; Olympus) at 40 × magnification and non-saturating conditions. Images were segmented using the DAPI staining to generate masks matching cell nuclei from which the corresponding signals were calculated using an in-house-developed package based on Cell Profiler.

RNA isolation and RT-qPCR

Cells were collected after two cold PBS washes by scraping in Tri-Reagent (Sigma-Aldrich). RNA was isolated by chloroform extraction followed by centrifugation, isopropanol precipitation, washing twice in 75% ethanol and resuspension in DEPC-treated water. Nucleic acid quantification was performed with a Nanodrop 8000 Instrument (Thermo Fisher Scientific). Reverse transcription reaction was carried out using High Capacity cDNA Reverse Transcription Kit (ABI), following the manufacturer's instructions, in a reaction volume of 20 μL and with Random primers contained in the kit. cDNA was stored at -20°C. For the detection on Telomeric repeat-containing RNA (TERRA), a first strand cDNA synthesis was first performed with the TERRA-specific RT-primer 5'-CCCTAACCC TAACCCTAACCCCTAACCCCTAA-3' [Feretzaki and Lingner, 2017](#) and a housekeeping gene-specific primer (Reverse) was included in the same reaction for normalization purposes. The reaction was carried out at 55°C in the presence of RNA inhibitor SUPERase IN (Thermo Fisher Scientific) using the SuperScript III RT (Thermo Fisher Scientific). qPCR was performed using the comparative CT method and a Step-One-Plus Real-Time PCR Instrument (Applied Biosystems). SYBR Green reactions were carried out in technical duplicate or triplicate in a final volume of 10 μL. For SYBR Green 1X SYBR Green PCR Master Mix (no. 4364344; ABI) or 1X SYBR Select Master Mix (no. 4472908; ABI), forward and reverse primer (Sigma; 100-500 nM each) and 25 ng of template were used. Thermocycling parameters used were: 95°C 20 s; 40 cycles 95°C 3 s, 60°C 30 s; melting curve. The 2-*ddCT* method was used for the analysis of the amplification products. Primer pairs used are indicated in [Table S6](#).

ATAC-seq and -qPCR

The Assay for Transposase-Accessible Chromatin (ATAC) protocol was adapted from [Buenrostro et al. \(2013\)](#). U-2-OS or HeLa LT cells were transfected in biological duplicate with siRNAs (siCont, siTLK1, siTLK2, siTLK1+2 for U-2-OS, and siCont, siTLK2 for HeLa LT WT and ΔTLK1) and 48 hours post-transfection were collected by trypsinization and counted. 50 000 cells for U-2-OS or 75 000 cells for HeLa LT were resuspended in 50 μL of cold lysis buffer (10 mM Tris-HCl, pH 7.4, 10 mM NaCl, 3 mM MgCl₂, 0.1% (v/v) Igepal CA-630) for nuclei preparation and treated with Nextera Tn5 Transposase (Nextera DNA Library Preparation Kit, Illumina) at 37°C for 30 min. DNA was first purified using MinElute PCR Purification Kit (QIAGEN). Samples were amplified by PCR using NEBNext High-Fidelity 2x PCR Master Mix (NEB) using PCR primers Ad1_noMX and Ad2_Barcode (Sigma-Aldrich, see [Table S6](#); [Buenrostro et al., 2013](#)) for 5 initial cycles (1 cycle: 5 min 72°C, 30 s 98°C; 5 cycles: 10 s 98°C, 30 s 63°C, 1 min 72°C). A qPCR side reaction was run on a tenth of the previous 5-cycle sample in order to determine the appropriate number of PCR cycles (N) and be able to stop amplification prior to saturation, in the presence of SYBR Green in an Applied Biosystems 7900HT Fast Real-Time PCR System (1 cycle: 30 s 98°C; 20 cycles: 10 s 98°C, 30 s 63°C, 1 min 72°C). Then, the 5-cycle sample was run for an additional N = 6 cycles, so the library had been amplified for a total of 11 cycles. Amplified libraries were purified using PureLink PCR Purification Kit (Thermo Fisher Scientific). The quality of purified libraries was assessed using a Bioanalyzer High-Sensitivity DNA Analysis kit (Agilent) where fragment size showed a periodical distribution of approximately 150-300-600-1200 bp. For ATAC-seq, an equimolar pool was generated and the pool was sequenced in 2 lanes 50 nt paired-end in an Illumina HiSeq2500 (Illumina). ATAC-qPCR was performed with the primers indicated on [Table S6](#) on a 1:20 dilution of the eluted DNA after library amplification.

For ATAC-seq analysis, paired end reads of length 50 bp were aligned to the human genome version hg19 using bowtie v0.12.9 ([Langmead et al., 2009](#)) with default parameters except for n = 1 to limit the maximum number of mismatches in the seed and m = 1 to report the best possible alignment for a given read. Alignments were sorted and indexed using Sambamba v0.5.8 (<http://lomereiter.github.io/sambamba/>). Duplicated reads were removed using Sambamba. Peaks were called with MACS v1.4.2 ([Zhang et al., 2008](#)) for each sample without any control. All parameters were left as default except for read length. Peaks were annotated with the HOMER v2.8.2 ([Heinz et al., 2010](#)) software with the hg19 annotations. Consensus peaks were defined as the union of all peaks from all biological samples. For each sample, the number of reads per peak was computed using the countBam function from the Rsamtools R package (version 1.30.0, <http://bioconductor.org/packages/release/bioc/html/Rsamtools.htm>). Differential accessibility was computed using DESeq2 ([Love et al., 2014](#)) with replicate as covariate. For ATAC-seq overlap with epigenetic marks, epigenetic information was downloaded from the Encode website ([Harrow et al., 2012](#)) (H3K9me3 [ENCFF001VDL]). Consensus peaks were classified according to their overlap with each epigenetic track [minimum overlap length 100bp]. P values were computed with a Mann-Whitney test as implemented in the function wilcox.test in R [R Core Team, 2016](#). For ATAC-seq FC correlation between replication time and methylation marks, the Repliseq track (wgEncodeUwRepliSeqNhekWaveSignalRep1.bigWig) was downloaded from the Encode website in Bigwig format. H3K36me3 and H3K9me3 corresponding to the U-2-OS cell line were also downloaded in

Bigwig format from the same repository. Mean normalized signal was computed for 10kb bins along the genome. Spearman correlations coefficients were computed with the `cor` function in R. For Figure S1D, Repliseq scores were binned in 25 quantiles. For ATAC-seq FC overlap with colors of chromatin, tracks were downloaded from Encode (`wgEncodeAwgSegmentation ChromhmmHellas3.bed`) corresponding to the ChromHMM algorithm (Ernst and Kellis, 2012) in the HeLa-S3 cell line. Peaks were classified to the color with larger overlapping segment. For better visualization, colors were collapsed to 10 classes as follows: Active Promoter = {Tss, TssF}, Promoter Flanking = {PromF}, Inactive Promoter = {PromP}, Candidate Strong enhancer = {Enh, EnhF}, Candidate Weak enhancer/DNase = {EnhWF, EnhW, DnaseU, DnaseD, FaireW}, Distal CTCF/CandidateInsulator = {CtcfO, Ctcf}, Transcription associated = {Gen5, Elon, ElonW, Gen3, Pol2, H4K20}, Low activity proximal to active states = {Low}, Polycomb repressed = {ReprD, Repr, ReprW}, Heterochromatin/Repetitive/Copy Number Variation = {Quies, Art}.

Chromatin immunoprecipitation (ChIP)

U-2-OS cells were transfected in biological duplicate with siRNAs (siCont and siTLK1+2) and 48 hours post-transfection were harvested by trypsinization. Cells were crosslinked with 1% formaldehyde in DMEM for 10 min at room temperature and quenched with glycine at a final concentration of 125 mM. Cells were washed with PBS, pelleted by centrifugation and dry pellets were snap frozen. For nuclear extract preparation, pelleted cells were thawed on ice, resuspended in cold Swelling buffer (25 mM HEPES pH 7.9, 1.5 mM MgCl₂, 10 mM KCl, 0.1% NP-40, 1x protease (Roche) and phosphatase inhibitors (Sigma-Aldrich)) for 10 min and passed through a douncer 50 times. Nuclei were pelleted by centrifugation at 3000 g for 5 min at 4°C, and resuspended in 300 μl of 1% SDS in ChIP buffer (10 mM Tris-HCl pH 7.5, 150 mM NaCl, 1% Triton X-100, 5 mM EDTA, 0.5 mM DTT, 1x protease (Roche) and phosphatase inhibitors (Sigma-Aldrich)). The extracts were incubated for 15 min on ice and sonicated in a Bioruptor Pico sonication device (Diagenode) for 30 cycles 30'' on/30'' off. Chromatin was cleared by centrifugation at top speed 15 min at 4°C and checked for size after a phenol/chloroform extraction by an agarose gel and by a Bioanalyzer DNA HS Chip (Agilent; Integrated Sciences) so chromatin fragments have a size of 200 bp on average. For H3.3 (Millipore 09-838) and H3K9me3 (Abcam ab8898) ChIP, 5 μg of total chromatin was diluted 1:10 in ChIP buffer and incubated with 1 μg of antibody on rotation at 4°C overnight. 50 μl of prewashed Dynabeads Protein G (Thermo Fisher Scientific) were added on rotation for 2h at 4°C. Beads were washed with Low Salt buffer (50 mM HEPES pH 7.5, 140 mM NaCl, 1% Triton X-100, 1x protease (Roche) and phosphatase inhibitors (Sigma-Aldrich)), High Salt buffer (50 mM HEPES pH 7.5, 500 mM NaCl, 1% Triton X-100, 1x protease (Roche) and phosphatase inhibitors (Sigma-Aldrich)) and eluted by incubating in a thermomixer with Elution buffer (1% SDS, 100 mM NaHCO₃) for 30 min at 65°C and 1000rpm. Samples were reverse-crosslinked by incubating at 65°C overnight and incubated with Proteinase K for 1h at 45°C. Chipped DNA was purified using the MinElute PCR Purification Kit (QIAGEN) and eluted in 40 μl. Purified ChIP DNA was used for library generation using the NEBNext Ultra II DNA Library Prep Kit for Illumina (NEB) following manufacturer's instructions. Each of the libraries was labeled by a specific barcode provided in NEBNext Multiplex Oligos for Illumina (Index Primers Set 1 and 2) (NEB) and amplified 9–13 cycles (depending on initial material amount) by PCR in the presence of SYBR Green in order to obtain an optimal yield. Libraries were quantified using DNA HS Qubit (Thermo Fisher Scientific) and size measured by a 2100 Bioanalyzer Instrument (Agilent) and a DNA HS Chip (Integrated Sciences). An equimolar pool was sequenced in 2 lanes 50 nt single read in an Illumina HiSeq2500 (Illumina). Libraries were also used as a template for qPCR using the primers corresponding to telomeric repeats (Tel) listed in Table S6.

For ChIP-seq analysis, single end reads of 50 bp length were aligned to the hg19 human genome version using Bowtie v0.12.9 (Langmead et al., 2009) with default parameters. Alignments were sorted and indexed using Sambamba v0.5.8 (<http://lomeriteir.github.io/sambamba/>). Duplicated reads were removed using Sambamba. Peaks were called with MACS v1.4.2 (Zhang et al., 2008) for each sample with the corresponding input as control. All parameters were left as default except for read length. Peaks were annotated with the HOMER v2.8.2 (Heinz et al., 2010) software with the hg19 annotations. Consensus peaks were defined as the union of all peaks from all samples. For each sample, the number of reads per peak was computed using the countBam function from the Rsamtools R package (version 1.30.0, <http://bioconductor.org/packages/release/bioc/html/Rsamtools.htm>). Differential binding was computed using DESeq2 (Love et al., 2014) with replicate as covariate. Normalized densities for peaks were computed using the annotatePeaks function from the HOMER suite. Densities were plotted using the feature AlignedDistribution function from the ChIPpeakAnno R package (Zhu et al., 2010).

RNA-seq

U-2-OS cells were transfected in biological duplicate with siRNAs (siCont, siTLK1, siTLK2, siTLK1+2) and 48 hours post-transfection were washed twice with cold PBS and collected by scraping in Tri-Reagent (Sigma-Aldrich). RNA was isolated using the PureLink RNA Mini Kit (Thermo Fisher Scientific) following the manufacturer's instructions for TRIzol Plus Total Transcriptome Isolation. Briefly, chloroform extraction followed by centrifugation resulted in a colorless upper aqueous phase that was mixed 1:1 with 100% ethanol. Sample containing RNA in 50% ethanol was bound to the spin cartridge, washed twice with Wash Buffer II and eluted in RNase-free water.

To avoid limiting our analysis in mRNA polyA+, we performed enrichment of whole transcriptome RNA by depleting ribosomal RNA (rRNA) species. Purified RNA samples were first quantified for integrity, size, and purity by a 2100 Bioanalyzer Instrument (Agilent) and an RNA 6000 Nano Chip (Integrated Sciences). 2 μg of total RNA were processed for rRNA depletion by Ribozero Gold rRNA Removal kit (Human/Mouse/Rat) (Illumina) following manufacturer's instructions. rRNA-free RNA was subsequently fragmented and cDNA generated by NEBNext RNA First Strand Synthesis Module (NEB) and NEBNext mRNA Second Strand Synthesis Module (NEB).

Resulting cDNA was purified, quantified, and used for library generation for Next Generation Sequencing using the NEBNext Ultra II DNA library prep for Illumina (NEB). Each of the libraries was labeled by a specific barcode provided in NEBNext Multiplex Oligos for Illumina (Index Primers Set 1) (NEB) and amplified 7 cycles by PCR in the presence of SYBR Green in order to obtain an optimal yield. Libraries were quantified using DNA HS Qubit (Thermo Fisher Scientific) and size measured by a 2100 Bioanalyzer Instrument (Agilent) and a DNA HS Chip (Integrated Sciences). An equimolar pool was generated with the eight libraries and the pool was sequenced in 2 lanes 50 nt single read in an Illumina HiSeq2500 (Illumina).

Single end reads of length 50 bp were aligned to the human genome version hg19 using bowtie v0.12.9 (Langmead et al., 2009) with default parameters. Alignments were sorted and indexed using Sambamba v0.5.8 (<http://lomereiter.github.io/sambamba/>). Gene differential expression was performed using DESeq2 (Love et al., 2014) with replicates as covariate. Pathway enrichment was assessed through the preranked version of Geneset Enrichment Analysis (GSEA) (Subramanian et al., 2005). GSEA was applied to the ranking defined by the log₂ Fold Change of the differential expression analysis using DESeq2. Genesets for analyses were from the Gene Ontology (GO) terms (Ashburner et al., 2000) as collected in the GSEABase R package (version 1.40.1), or from the Hallmark collection (Liberzon et al., 2015) after retrieval from the MsigDB (Liberzon et al., 2011). Classification in coding and noncoding gene classes was performed according to the Gencode annotation version 19 (Harrow et al., 2012). For Repeat Masker analysis, sequences from repeat elements in the human Repbase database version 22.06 (Bao et al., 2015) were downloaded. Reads were aligned using bowtie with parameters `-best` and `-k = 1`. Fold changes were computed between siTLK1+2 and siCont samples using normalized reads values of those repeat sequences that had at least 100 raw reads.

C-circle assay

The C-circle assay protocol was adapted from Henson et al. (2017). Genomic DNA from 200 000 cells was extracted by incubating cells with 50 μ l of QCP lysis buffer (50 mM KCl, 10 mM Tris-HCl pH 8.5, 2 mM MgCl₂, 0.5% IGEPAL CA-630, 0.5% Tween-20) and 3 μ l of QIAGEN protease shaking at 1400 rpm at 56°C for 1 hour. The QIAGEN protease was inactivated by incubating the samples at 70°C for 20 min. DNA concentration was measured by fluorimetry using the Qubit dsDNA HS Assay (Thermo Fisher Scientific). Samples purified from U-2-OS and HeLa LT cells were pre-diluted in QCP lysis buffer at 5 ng/ μ l and 30 ng/ μ l, respectively. 5 or 30 ng of DNA were diluted to 10 μ l in 10mM Tris-HCl pH 7.6 and mixed with 9.25 μ l of Rolling Circle Master Mix (RCMM) (8.65mM DTT, 2.16X 10X ϕ 29 Buffer, 8.65ug/mL BSA, 0.216% Tween-20 and 2.16mM of each dATP, dCTP, dGTP and dTTP) and 0.75 μ l of ϕ 29 DNA Polymerase (NEB or Thermo Fisher Scientific). Rolling Circle Amplification was performed by incubating samples in a thermocycler at 30°C for 8 hours, polymerase was inactivated at 70°C for 20 min and then kept at 8-10°C. Samples were kept at -20°C. For slot blot detection, samples were diluted with 2x SSC to 200 μ l, then slot-blotted onto Nytran SuPerCharge (SPC) nylon blotting membranes (Sigma-Aldrich) under native conditions. After 254 nm UV-C crosslinking, the membrane was hybridized with γ -³²P labeled Tel-C oligo probe (CCCTAA)₄ in hybridization buffer (1.5X SSPE, 10% polyethylene glycol (PEG) MW 8000, 7% SDS) for 16 h. Membrane was exposed onto a storage phosphor screen (Molecular Dynamics) and scanned using Typhoon 8600 Variable Mode Imager (Molecular Dynamics). Membrane was stripped in wash solution (0.5X SSC, 0.1% SDS) at 65°C and re-hybridized with γ -³²P labeled Alu oligo probe for loading control.

Analysis of TCGA signatures

TCGA RNA-Seq datasets were downloaded from the legacy archive of the NCI GDC commons database (Grossman et al., 2016) and processed separately for each cancer type. Expression measures were expressed in RSEM (Li and Dewey, 2011) in this TCGA version, which were log₂-transformed and quantile normalized. For patients with multiple instances, a single sample chosen at random was kept while the rest were excluded from further analyses. For a number of cancer types there were two different platforms available: Illumina HiSeq 2000 (HiSeq) and Illumina Genome Analyzer (GA); in such cases, duplicated samples across platforms were removed from the GA dataset while the HiSeq instance was kept in the final dataset. Samples whose expression values showed an unusual distribution compared to the rest of samples in their datasets were also excluded (ACC: TCGA-OR-A5L9-01A; HNSC: TCGA-D6-A6ES-01A and TCGA-CV-A45Q-01A; LAML: TCGA-AB-2955-03A, TCGA-AB-2986-03A, TCGA-AB-2816-03A, TCGA-AB-2955-03A, TCGA-AB-2986-03A and TCGA-AB-2816-03A; LIHC: TCGA-DD-A3A6-11A and TCGA-FV-A4ZP-01A; SKCM: TCGA-D3-A2JK-06A; UCEC: TCGA-BS-A0V4-01A; UVM: TCGA-WC-A885-01A; COAD: TCGA-A6-2679-01A and TCGA-AA-A004-01A). For each cancer type, expression matrices were corrected a-priori by platform, source center, and plate id, when suitable. For doing so, a linear model was fitted to the expression values gene wise in which platform and source center were included as fixed effects. Regarding sample's plate id, it was included in the models as a fixed or a random effect depending on the number of levels and sample size available for the cancer type under consideration. In some cases, additional variables were also included in the models in order to preserve signal with biological or clinical relevance (BLCA: diagnosis subtype; BRCA: PAM50 subtype; COAD and STAD: microinstability status; KIRP: tumor type).

Aneuploidy score and Stromal and Leukocyte fraction estimates were obtained from Taylor et al. (2018). To estimate chromosomal instability (CIN) we computed signatures with the gene set CIN25 published in Carter et al. (2006). ALT status was taken from Lee et al. (2018a). Gene signature scores were computed as the mean of all genes in the signature after scaling the expression matrix gene wise. The global signature was defined as the score associated with the gene signature containing all genes in the expression matrix. Correlation coefficients and p values were computed using the 'pcor.test' function from the ppcor R package (Kim, 2015). In order to

avoid spurious correlations due to technical and global effects (Caballé Mestres et al., 2018), partial correlations were computed whenever a gene signature was involved with the global signature as adjusting variable.

For the association between ALT status and signatures, expression matrices for all available TCGA datasets were scaled gene wise and merged. Only those cancer types with more than two ALT+ patients were included in the merged dataset. In order to account for possible technical and global effects, gene signature scores were adjusted by the global signature before plotting (Caballé Mestres et al., 2018). P values and coefficients of the association between gene expression or gene signatures and ALT status were computed through a linear model with the dataset as covariable. Whenever gene signatures were being tested, the global signature was also included as covariable. The scores associated to stromal fraction, leukocyte fraction, and aneuploidy were transformed using the square root to ensure normality of the data for the linear model. P values were adjusted for multiple comparisons using Benjamini-Hochberg.

QUANTIFICATION AND STATISTICAL ANALYSIS

Statistical significance of non-sequencing experiments was determined with the tests stated in the figure legends using PRISM software (GraphPad Software Inc.). All data are from a minimum of two independent experiments. Specific biological replicate numbers (n) for each experiment can be found in the corresponding figure legends. Statistical analysis of ATAC-seq FC were computed with a Mann-Whitney test as implemented in the function `wilcox.test` in R. Statistical analysis of TCGA datasets is described in detail in the corresponding methods section. Statistically significant differences are labeled with one, two, three or four asterisks if $p < 0.05$, $p < 0.01$, $p < 0.001$ or $p < 0.0001$, respectively.